

# Orientation dependence of shear banding in face-centered-cubic single crystals

N. Jia<sup>a,b</sup>, P. Eisenlohr<sup>b</sup>, F. Roters<sup>b</sup>, D. Raabe<sup>b,\*</sup>, X. Zhao<sup>a</sup>

<sup>a</sup> Key Laboratory for Anisotropy and Texture of Materials (MOE), Northeastern University, Shenyang 110004, China

<sup>b</sup> Max-Planck-Institut für Eisenforschung, D-40237 Düsseldorf, Germany

Received 19 February 2012; received in revised form 2 March 2012; accepted 3 March 2012

Available online 6 April 2012

## Abstract

We present crystal plasticity finite element simulations of plane strain compression of  $\alpha$ -Brass single crystals with different initial orientations. The aim is to study the fundamentals of mesoscale structure and texture development in face-centered-cubic (fcc) metals with low stacking fault energy (SFE). Shear banding depends on the initial orientation of the crystals. In Copper and Brass-R-oriented crystals which show the largest tendency to form shear bands, an inhomogeneous texture distribution induced by shear banding is observed. To also understand the influence of the micromechanical boundary conditions on shear band formation, simulations on Copper-oriented single crystals with varying sample geometry and loading conditions are performed. We find that shear banding can be understood in terms of a mesoscopic softening mechanism. The predicted local textures and the shear banding patterns agree well with experimental observations in low SFE fcc crystals.

© 2012 Acta Materialia Inc. Published by Elsevier Ltd. All rights reserved.

**Keywords:** Fcc material; Shear band; Texture; Crystal plasticity finite element analysis

## 1. Introduction

Shear bands, in the form of non-crystallographic band-like regions of concentrated plastic flow, are one of the most frequently observed yet least understood microstructural features in plastically strained face-centered-cubic (fcc) metallic materials [1–8]. They are characterized by massive collective dislocation activity in a narrow local deformation zone while the abutting matrix undergoes comparably homogeneous flow. Shear banding is promoted when homogeneous dislocation slip is inhibited [9]. In such cases shear banding can act as an alternative and mesoscopically non-crystallographic deformation mode, often associated with a sudden drop in the local flow stress. The stacking fault energy (SFE) plays an important intrinsic role in that context as it influences the formation of strong obstacles [1,8,10–14]. For fcc materials with high

or medium SFE, typical microstructure obstacles are elongated dislocation walls and cell blocks. Shear bands in such materials are classified as Copper-type shear bands. The resulting crystallographic texture associated with Copper-type shear bands are the  $\{112\}\langle 111 \rangle$  (Copper) and  $\{123\}\langle 634 \rangle$  (S) texture components (Copper-type textures) and  $\{011\}\langle 100 \rangle$  (Goss) texture components [8,11,15]. In contrast, in low SFE materials shear banding is preceded by the blockage of dislocation slip by twin-matrix lamellae at an early stage of deformation. Since the mesoscopic alignment of shear bands differs from the  $\{111\}$  slip plane, deformation inside the shear band is often referred to as being non-crystallographic [1,4,10,13,14]. In this case, shear bands are classified as Brass-type. The resulting textures are characterized by the Goss and  $\{011\}\langle 211 \rangle$  (Brass) texture components (Brass-type texture). In either case, shear banding is initiated by a mechanical instability that contains band-like dislocation cells or twin-matrix lamellae as well as high local orientation changes at the border between the band and the matrix [16]. Many high SFE

\* Corresponding author.

E-mail address: [d.raabe@mpie.de](mailto:d.raabe@mpie.de) (D. Raabe).

metals, e.g. pure aluminum, deform more homogeneously even at high plastic strains due to the extensive dynamic recovery in these materials; hence, they develop Copper-type textures [17,18]. These lead to a conclusion that in materials with low SFE, shear banding has a decisive effect on the texture transition from the Copper to the Brass type [14,19]. The development of Brass-type shear bands is associated with two important microstructure phenomena. One is the effect of shear bands on local texture evolution with increasing strain. The other is their role in transforming the twin-matrix lamellae to a nanoscaled structure inside the bands. Local orientation measurements using transmission electron microscopy (TEM) reveal that shear bands cut through profuse fine twins, following which a lattice rotation different from that caused by dislocation and twinning shear occurs within the bands [20,21]. Regarding the microstructural aspect, recent experiments employing high-resolution TEM confirm a two-stage process of shear bands formation, i.e. a nucleation/initiation stage resulting in narrow bands composed of nanocrystals intersecting the twin layers, and a thickening stage of the bands into their adjacent twin-matrix regions [20].

In the past decades, various simulation studies on shear band formation and the associated texture evolution were carried out [22–34]. Based on plastic power minimization and maximum geometric softening considerations, the criterion  $d\sigma/d\varepsilon < 0$  where  $\sigma$  denotes the equivalent true stress and  $\varepsilon$  the equivalent true strain was identified as a condition for the initiation of localized deformation in early works [35,36]. Other approaches assumed that shear bands originate from unstable perturbations of the lattice orientation in a rigid-plastic single crystal [37,38]. Some studies emphasized that the development of shear bands during deformation depends on the mobility of dislocations associated with specific microstructures. Although these studies have profoundly improved our knowledge about shear banding, no theoretical concept exists that allows us to unambiguously predict: firstly, the process of shear banding in terms of an initiation and thickening process; secondly, the crystallographic orientation dependence of banding with respect to external and internal boundary conditions; and thirdly, how shear banding contributes to the resulting crystallographic texture. The reasons for the absence of a consistent theoretical concept have been ascribed to the lack of an incorporation of microstructure [39] and to an insufficient mapping of crystallographic aspects related to the phenomena [40].

Therefore, in this study, the development of shear bands in a low SFE fcc material ( $\alpha$ -Brass) is systematically studied as a function of orientation, constitutive behavior, and loading conditions. Plane strain compression of single crystal samples with different initial orientations is simulated using a crystal plasticity finite element (CPFE) model that incorporates the non-crystallographic shear banding mechanism in addition to dislocation slip and mechanical twinning [41]. Our aim is to predict the structure and texture development of the material undergoing shear banding.

We analyze the simulation results with respect to mechanical instability aspects, inhomogeneity of microstructures and plastic flow, orientation dependence, and effects of boundary conditions. More specifically, we conduct the following steps:

- By performing simulations with different constitutive models on differently oriented single crystals, the effects of initial orientation on shear banding are investigated.
- For each single crystal we analyze the resulting textures in regions of strain localization. Predictions of local texture evolution in Copper-oriented fcc crystals are compared in detail to published experiments.
- As Copper-oriented crystals have a strong tendency to form shear bands, systematic simulations for this orientation are performed on samples with varying aspect ratios and boundary conditions.

## 2. Simulation procedure

### 2.1. Basic considerations on constitutive modeling of shear bands

A CPFE model is used to simulate the evolution of microstructure and texture in  $\alpha$ -Brass (Cu–30 wt.% Zn) single crystals during plane strain compression. The model is based on a constitutive model that incorporates shear banding as a separate non-crystallographic mechanism in conjunction with dislocation slip and mechanical twinning. Alternatively, simulations can be conducted by activating only one or two out of these three competing mechanisms (intrinsic shear banding, dislocations, deformation twins). The implementation of dislocation glide and twinning follows the approaches presented recently by Jia et al. [41]. The implementation of shear banding as a third deformation mechanism is motivated by the experimental observation that shear bands develop with a non-crystallographic geometry when normal crystallographic slipping is inhibited by the twin-matrix structures [1,4,5,8,13,14]. We apply here the continuum shear band approach originally developed for amorphous metallic materials [42] to simulate shear banding in crystalline matter as already used in a preceding study on texture evolution in fcc polycrystals [41].

### 2.2. Constitutive formulations

#### 2.2.1. Flow rule

We use the finite strain kinematic framework in which the deformation gradient,  $\mathbf{F}$ , is multiplicatively decomposed according to:

$$\mathbf{F} = \mathbf{F}^e \mathbf{F}^p \quad (1)$$

where  $\mathbf{F}^e$  is the elastic part comprising the stretch,  $\mathbf{U}^e$ , and the lattice rotation,  $\mathbf{R}^e$ ;  $\mathbf{F}^p$  is the plastic part of the deformation gradient. The initial plastic deformation gradient  $\mathbf{F}_0^p$  is set to the inverse of the local crystal orientation,

$T_0^{-1}$ , and evolves at a rate governed by the plastic velocity gradient  $\mathbf{L}^P$ :

$$\dot{\mathbf{F}}^P = \mathbf{L}^P \mathbf{F}^P \quad (2)$$

As plastic deformation alone does not alter the crystal lattice orientation its evolution with strain can be calculated from the polar decomposition  $\mathbf{F}^e = \mathbf{R}^e \mathbf{U}^e$  as  $\mathbf{T} = \mathbf{R}^e$ . Inspired by Kalidindi [43], the plastic velocity gradient,  $\mathbf{L}^P$ , has contributions from 12  $\{111\}\langle 110 \rangle$  dislocation slip systems, 12  $\{111\}\langle 112 \rangle$  twinning systems, and the extra six shear band systems:

$$\mathbf{L}^P = \sum_{\alpha=1}^{12} \dot{\gamma}^{\alpha} \mathbf{m}^{\alpha} \otimes \mathbf{n}^{\alpha} + \sum_{\beta=1}^{12} \dot{\gamma}^{\beta} \mathbf{m}_{\text{twin}}^{\beta} \otimes \mathbf{n}_{\text{twin}}^{\beta} + \sum_{\gamma=1}^6 \dot{\gamma}^{\gamma} \mathbf{m}_{\text{sb}}^{\gamma} \otimes \mathbf{n}_{\text{sb}}^{\gamma} \quad (3)$$

The vectors  $\mathbf{m}$  and  $\mathbf{n}$  denote the directions and plane normals of the deformation systems on which shear occurs at a rate of  $\dot{\gamma}$ . By omitting the volume fraction of the non-twinned crystal portions in the contribution of dislocation slip in Eq. (3) (in contrast to Ref. [43]), we (i) assume that twins can be further sheared by dislocation slip in a compatible manner to the surrounding matrix, and (ii) ignore any potentially different evolution of slip resistance within them.

### 2.2.2. Dislocation slip and mechanical twinning

Conventional flow rules use a reference shear rate and a rate sensitivity exponent, which are typically constant [34]. In this paper, however, following the work of Blum and Eisenlohr [44], the evolution of dislocation densities is related to dislocation multiplication, dipole formation and dislocation annihilation. The flow rule describes thermally activated dislocation motion through forest dislocations. The shear rate of the slip system  $\alpha$  is:

$$\dot{\gamma}^{\alpha} = \rho_{\text{sgl}}^{\alpha} b v_0 \exp \left[ \left( -\frac{Q_0}{k_B T} \left( 1 - \frac{|\tau^{\alpha}|}{\hat{\tau}^{\alpha}} \right)^p \right)^q \right] \text{sign}(\tau^{\alpha}) \quad (4)$$

where  $\tau^{\alpha}$  is the current resolved shear stress;  $\hat{\tau}^{\alpha}$  is the slip resistance governed by the dislocation population;  $\rho_{\text{sgl}}^{\alpha}$  is the unipolar dislocation density;  $b$  is the length of the Burgers vector;  $v_0$  is the dislocation velocity of the slip system when subjected to a stress equal to the slip resistance  $\hat{\tau}^{\alpha}$ ;  $Q_0$  is the activation energy for dislocation slip;  $k_B$  and  $T$  denote the Boltzmann constant and temperature, respectively;  $p$  and  $q$  are numerical parameters to adjust the obstacle profile [45]. The slip resistance  $\hat{\tau}^{\alpha}$  depends on the local dislocation densities as:

$$\hat{\tau}^{\alpha} = \tau_{\text{solute}} + Gb \left( \sum_{\alpha'=1}^{N_{\text{slip}}} \xi_{\alpha\alpha'} \left( \rho_{\text{sgl}}^{\alpha'} + \rho_{\text{dip}}^{\alpha'} \right) \right)^{1/2} \quad (5)$$

with  $\tau_{\text{solute}}$  a constant resistance from solid solution,  $G$  the shear modulus,  $\rho_{\text{dip}}^{\alpha'}$  the dipolar dislocation density, and  $\xi_{\alpha\alpha'}$  characterizes the interaction strength between different slip systems  $\alpha$  and  $\alpha'$  as a result of the possible interaction types of self, coplanar, collinear, orthogonal, glissile and sessile [46].

Based on the twin nucleation model proposed by Mahajan and Chin [47], it is assumed that the critical twin nucle-

ation event consists in the correlated bow-out of three partial dislocations between pinning points separated by  $L_0$ . Then, the critical stress for twin formation is calculated as

$$\hat{\tau}_{\text{twin}} = \frac{\gamma_{\text{sf}}}{3b_{\text{twin}}} + \frac{3Gb_{\text{twin}}}{L_0} \quad (6)$$

where  $b_{\text{twin}}$  is the magnitude of the Burgers vector of the moving partials and  $\gamma_{\text{sf}}$  is the stacking fault energy of the material. Using this critical stress the twin nucleation rate is expressed as

$$\dot{N}^{\beta} = \dot{N}_0 \exp \left[ - \left( \frac{\hat{\tau}_{\text{twin}}}{\tau^{\beta}} \right)^r \right] \quad (7)$$

where  $\tau^{\beta}$  is the resolved stress in twin system  $\beta$ , and  $\dot{N}_0$  and  $r$  are fitting parameters. It should be mentioned that for dislocation slip, the rate equation of the dislocation multiplication is in the form  $d\rho = \frac{|\dot{\gamma}^{\alpha}|}{b\lambda^{\alpha}}$ , where  $\lambda^{\alpha}$  is the effective spacing between obstacles. With the presence of twins  $\lambda^{\alpha}$  has to include twin boundaries as additional obstacles to dislocation motion. The slip–twin interaction parameter  $\xi_{\alpha\beta}$  is hence introduced for the interaction between slip system  $\alpha$  and twin system  $\beta$ . If planes  $\alpha$  and  $\beta$  are coplanar or  $\beta$  is a cross-slip plane for  $\alpha$ ,  $\xi_{\alpha\beta}$  is 0. In other cases  $\xi_{\alpha\beta}$  is equal to 1. Finally, the mean free path of dislocations is calculated as

$$\frac{1}{\lambda^{\alpha}} = \frac{1}{d_{\text{grain}}} + \sum_{\beta=1}^{N_{\text{twin}}} \xi_{\alpha\beta} \frac{1}{d_{\text{twin}}^{\beta}} \quad (8)$$

where  $d_{\text{grain}}$  is the constant grain size, and  $d_{\text{twin}}$  evolves with twin volume fractions as:

$$d_{\text{twin}}^{\beta} = s(1-f)/f^{\beta} \quad (9)$$

with  $s$  a constant twin thickness,  $f$  the total volume fraction of twins and  $f^{\beta}$  the volume fraction of a specific twin system. Details of the dislocation and twinning models are described in Refs. [41,44,45].

### 2.2.3. Shear banding

The incorporation of shear banding into the constitutive model is motivated by the fact that non-crystallographic shear zones occur in low SFE alloys when dislocation slip is inhibited, e.g. by the presence of dense twin boundaries as frequently observed in experiments [1,4,5,8,13,14]. The shear banding mechanism suggested by Anand and Su [42] for amorphous materials and by Wei et al. [48] for nanocrystalline materials is adopted in this work. In this approach, the potential shear band systems, defined relative to the three (variable) principal directions of the second Piola–Kirchhoff stress  $\mathbf{T}^e$  (conjugated to the elastic Green–Lagrange strain), are introduced when the critical stress for shear band formation is reached at one material point. The decomposition of the Piola–Kirchhoff stress  $\mathbf{T}^e$  is:

$$\mathbf{T}^e = \sum_{i=1}^3 \sigma_i \hat{\mathbf{e}}_i \otimes \hat{\mathbf{e}}_i \quad (10)$$

where  $\sigma_i$  are the principal stresses and  $\hat{\mathbf{e}}_i$  the orthonormal principal directions of  $\mathbf{T}^e$ . Plastic flow due to shear banding is considered on six potential systems in those (non-crystallographic) planes that are constructed by the three principal stress directions. The potential shear band systems on the  $(\hat{\mathbf{e}}_i - \hat{\mathbf{e}}_j)$  planes are specified by a direction  $\mathbf{m}$ , and a plane normal  $\mathbf{n}$ :

$$\begin{aligned}\mathbf{m}^{(1)} &= \cos \theta \hat{\mathbf{e}}_1 + \sin \theta \hat{\mathbf{e}}_3, \quad \mathbf{n}^{(1)} = \sin \theta \hat{\mathbf{e}}_1 - \cos \theta \hat{\mathbf{e}}_3 \\ \mathbf{m}^{(2)} &= \cos \theta \hat{\mathbf{e}}_1 - \sin \theta \hat{\mathbf{e}}_3, \quad \mathbf{n}^{(2)} = \sin \theta \hat{\mathbf{e}}_1 + \cos \theta \hat{\mathbf{e}}_3 \\ \mathbf{m}^{(3)} &= \cos \theta \hat{\mathbf{e}}_1 + \sin \theta \hat{\mathbf{e}}_2, \quad \mathbf{n}^{(3)} = \sin \theta \hat{\mathbf{e}}_1 - \cos \theta \hat{\mathbf{e}}_2 \\ \mathbf{m}^{(4)} &= \cos \theta \hat{\mathbf{e}}_1 - \sin \theta \hat{\mathbf{e}}_2, \quad \mathbf{n}^{(4)} = \sin \theta \hat{\mathbf{e}}_1 + \cos \theta \hat{\mathbf{e}}_2 \\ \mathbf{m}^{(5)} &= \cos \theta \hat{\mathbf{e}}_2 + \sin \theta \hat{\mathbf{e}}_3, \quad \mathbf{n}^{(5)} = \sin \theta \hat{\mathbf{e}}_2 - \cos \theta \hat{\mathbf{e}}_3 \\ \mathbf{m}^{(6)} &= \cos \theta \hat{\mathbf{e}}_2 - \sin \theta \hat{\mathbf{e}}_3, \quad \mathbf{n}^{(6)} = \sin \theta \hat{\mathbf{e}}_2 + \cos \theta \hat{\mathbf{e}}_3\end{aligned}\quad (11)$$

with  $\theta = \pi/4$ .

To formulate a kinetic equation for shear band formation, we adopt the approach of Anand and Su [42] and Wei et al. [48], which is phenomenologically related to that used for crystallographic slip (Eq. (4)). This approach is sensible since a strain-softening criterion, which is also discussed for low SFE fcc alloys [20,21], introduces non-convexity into the constitutive law. This renders the softening criterion difficult to implement in the current framework due to convergence issues. Thus, the original governing condition for the “nucleation” of shear bands is modified from a diminishing strain-hardening criterion to a critical resolved stress criterion, i.e. a resistance to shear banding. The shear rate  $\dot{\gamma}^\chi$  for the shear band system  $\chi$  is formulated in analogy to that for dislocation slip systems:

$$\dot{\gamma}^\chi = \dot{\gamma}_0^\chi \exp \left[ \left( -\frac{Q_0}{k_B T} \left( 1 - \frac{|\tau^\chi|}{\hat{\tau}_{sb}} \right)^p \right)^q \right] \text{sign}(\tau^\chi) \quad (12)$$

where  $\dot{\gamma}_0^\chi$  is a reference shear rate,  $\tau^\chi$  is the resolved stress on system  $\chi$ , and  $\hat{\tau}_{sb}$  is the constant threshold stress for shear banding. It is worthwhile to mention that these shear rates just contribute to the plastic deformation velocity gradient  $\mathbf{L}^p$  of the crystal according to Eq. (3) and we do not treat the shear bands as extended objects with an orientation different from that of the matrix.

#### 2.2.4. Constitutive material parameters

The constitutive parameters are determined by fitting the macroscopic stress–strain ( $\sigma$ – $\varepsilon$ ) and the strain-hardening ( $d\sigma/d\varepsilon$ – $\sigma$ ) curves obtained from uniaxial compression tests of  $\alpha$ -Brass [49]. According to our recent work [41], the optimal parameters are:

- Single crystal elastic constants:  $C_{11} = 147$  GPa,  $C_{12} = 111$  GPa,  $C_{44} = 72$  GPa.
- Parameters regarding the motion and thermal activated annihilation of dislocations according to the constitutive equations in Section 2.2:  $d_{\text{grain}} = 30$   $\mu\text{m}$ ,  $s = 0.1$   $\mu\text{m}$ ,  $b = 2.56 \times 10^{-10}$  m,  $\tau_{\text{solute}} = 0.033$  GPa,  $Q_0 = 4.0 \times 10^{-19}$  J,  $p = 1.15$ ,  $q = 1.0$ . The initial dislocation density

$\rho_{\text{sgl},0}$  and dipole density  $\rho_{\text{dip},0}$  are taken as  $\rho_{\text{sgl},0} = 1.0 \times 10^{12}$  m $^{-2}$  and  $\rho_{\text{dip},0} = 1.0$  m $^{-2}$ . The bulk diffusion coefficient  $D_0$  is  $3.4 \times 10^{-5}$  m $^2$  s $^{-1}$ .

- Parameters regarding twin formation:  $b_{\text{twin}} = 1.47 \times 10^{-10}$  m,  $\gamma_{\text{sf}} = 0.015$  J m $^{-2}$ ,  $L_0 = 520 \times b$ ,  $\dot{N}_0 = 5.0 \times 10^{14}$  s $^{-1}$ ,  $r = 2.0$ .
- Parameters regarding initiation of the shear band systems:  $\dot{\gamma}_0^\chi = 1.0 \times 10^{-4}$  m s $^{-1}$ ,  $\hat{\tau}_{sb} = 0.18$  GPa.

#### 2.3. Application to fcc single crystals

Based on the constitutive laws outlined above, the CPFEE simulations are carried out using the finite element solver MSC.Marc2010 together with a user defined material subroutine. The present paper focuses on the deformation of four single crystals with initial Copper ((112)[11 $\bar{1}$ ]), cube ((100)[001]), Goss ((01 $\bar{1}$ )[100]) and Brass-R ((111)[11 $\bar{2}$ ]) orientations, respectively. In each model, the textured material is exactly oriented as ideal component, i.e. all elements have the same initial orientation without any orientation scatter. FE meshes with second-order isoparametric, six-noded, two-dimensional plane strain triangular elements are used. The same orientation (of the crystal) is assigned to each of the three integration points in an element. Fig. 1 shows the modeled region with thickness  $H_0$  and length  $L_0 = H_0/2$  (aspect ratio = 0.5) in a bulk material in an undeformed state. For simulating plane strain compression, the elongation direction (ED), normal direction (ND), and transverse direction (TD) are set to coincide with a Cartesian coordinate system,  $X$ ,  $Y$ , and  $Z$ , respectively. Aiming at an explicit understanding of the influence of initial orientation, sample geometry and boundary conditions on shear banding deformation, the simulations are divided into three groups:

- Group 1 (effect of initial orientation): single crystals with different initial orientations of Copper, cube, Goss and Brass-R; same thickness-to-length ratio of 0.5; a prescribed displacement corresponding to the thickness reduction is applied to the top edge with a strain rate of  $10^{-3}$  s $^{-1}$ . The right edge is free to move in the  $X$  direction. The left and bottom edges are constrained from moving in the  $X$  and  $Y$  directions, respectively. Multi-point constraints are applied to maintain the right edge straight during deformation. The boundary conditions are denoted hereafter as “Tie Right” and applied for all the simulations in this group. Simulations are performed using four models incorporating different specific deformation mechanisms: (i) dislocation slip only, denoted hereafter as “Slip” model; (ii) dislocation slip and mechanical twinning, denoted as “Slip + Twin” model; (iii) dislocation slip, twinning and shear banding, denoted as “Slip + Twin + SB” model; and (iv) dislocation slip and shear banding, denoted as “Slip + SB” model.



- Group 2 (effect of sample geometry): single crystal initially oriented as Copper orientation using different thickness-to-length ratios of 0.5, 0.67, 1.0 and 2.0. Here we use “Tie Right” boundary conditions. Slip + Twin + SB simulations are performed on crystals with different geometry.
- Group 3 (effect of boundary conditions): single crystals initially oriented as Copper orientation with a thickness-to-length ratio of 0.5. In addition to the boundary conditions described above, three other types of boundary conditions are adopted for each simulation: (i) without multi-point constraints on the right edge and other settings identical to “Tie Right”, denoted as “Relax Right”, (ii) without multi-point constraints on both left and right edges, nodes in the middle of the top and bottom edges could not move in the  $X$  direction. The other settings are the same as used for “Tie Right”, denoted as “Relax Both”, and (iii) periodic boundary conditions, denoted as “PBC”. Still, Slip + Twin + SB simulations are performed in this group.

### 3. Simulation results

#### 3.1. Group 1 (single crystals with different initial orientation but the same aspect ratio and boundary conditions)

##### 3.1.1. Mechanical response

The equivalent true stress–equivalent true strain curves of the single crystals obtained from models incorporating different deformation mechanisms are shown in Fig. 2. The onset of strain localization defined by the first appearance of a negative strain-hardening rate, i.e.  $d\sigma/d\varepsilon < 0$ , is marked by “○”, where  $\sigma$  and  $\varepsilon$  denote equivalent true stress and equivalent true strain, respectively. For the crystals with initial Copper and Brass-R orientations, the Slip + Twin + SB and Slip + SB models predict earlier strain localization (at a strain level below  $\sim 0.35$  for Copper, and below  $\sim 0.2$  for Brass-R) compared to the slip and Slip + Twin models (at a strain of  $\sim 0.4$  for Copper, and  $\sim 0.3$  for Brass-R). Because of the specific boundary conditions applied in the models, the strain localization is not caused by a distorted shape of the samples, as can be seen from the deformed configuration in Fig. 3. For cube, the shear band simulations (Slip + Twin + SB and Slip + SB) show that localization occurs at a strain above  $\sim 0.42$ , while the simulations without shear banding (slip and Slip + Twin) do not show localization until 0.8. For Goss-textured material, all simulations do not show strain localization.

Fig. 3 shows the distribution of equivalent logarithmic strain for each single crystal at 37% thickness reduction (0.46 strain). Since the slip and Slip + Twin models predict similar strain patterns and the Slip + Twin + SB model also predicts similar behavior as the Slip + SB model, only results obtained from the Slip + Twin and Slip + Twin + SB simulations are presented. For the Copper-textured material (Fig. 3a), pronounced strain localization

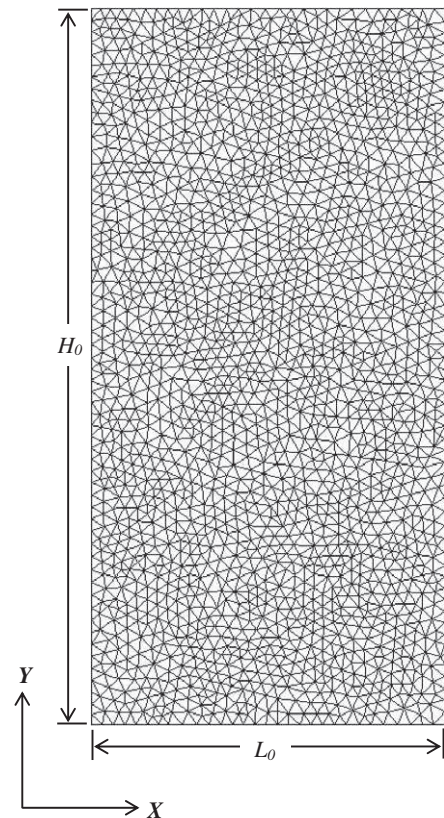


Fig. 1. Schematic of a single crystal model consisting of triangular elements. To simulate plane strain compression, a prescribed displacement corresponding to the thickness reduction is applied to the top edge. The left and bottom edges are constrained from moving in the  $X$  and  $Y$  directions, respectively. The right edge is permitted to move in the  $X$  direction.

(with the maximum variation of local strain among the constituent material points of  $\sim 3.0$ ) is predicted by both models. However, different strain patterns are observed: the Slip + Twin simulation shows that strain is localized between the top-left and bottom-right corners of the Copper-oriented crystal and the zone of high strain is inclined at  $\sim 44^\circ$  to ED; the Slip + Twin + SB model shows that the localized zone is between the left and right bounding edges of the crystal and forms an angle of  $\sim 39^\circ$  to ED. With the use of both models, pronounced strain localization is also predicted in the Brass-R crystal (Fig. 3d), while the cube and Goss-textured single crystals show very weak localization with a maximum strain variation below 0.15 (Fig. 3b and c).

Shear contributions of the competing deformation systems (dislocation slip, twinning, shear banding) obtained from the different simulations are plotted as a function of the equivalent true strain in Fig. 4. The individual contributions are given as summations over the absolute values of the shear rates on the different systems for each type of mechanism, and then, normalized by the overall shear in each time step. For the Copper-textured material (Fig. 4a), the following features are observed. The slip simulation shows that the shear rate on the slip systems gener-

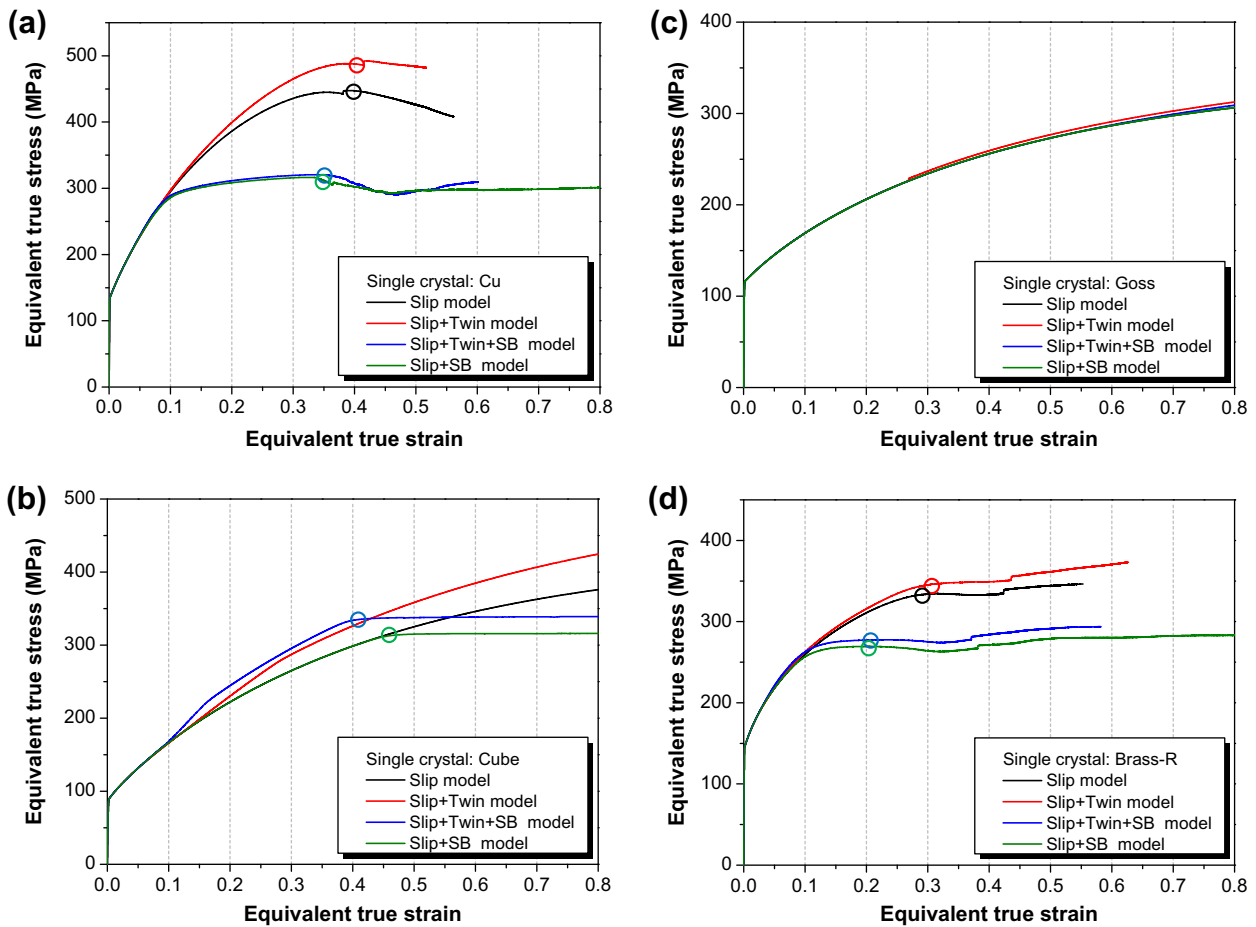


Fig. 2. Predicted stress–strain curves for single crystals with different initial crystallographic orientations during plane stress compression: (a) Copper, (b) cube, (c) Goss and (d) Brass-R.

ally remains on a constant level during plastic straining. For the simulation considering dislocations and twins (Slip + Twin model), an increase in the twinning shear rate is predicted at an initial stage of deformation, and the maximum occurs at a strain of 0.13. With further deformation, the shear rate carried by dislocations increases, indicating that the material is deformed both by slip and by twinning. For the Slip + Twin + SB simulation, at the initial stage of deformation dislocations and twins provide similar shear contributions as in the models without shear banding. At a strain of 0.07, the shear rate from dislocation slip drops and the shear rate contributed by shear banding increases, indicating that shear banding increasingly carries the deformation. When the strain reaches 0.15, the shear rate on the shear band systems is higher than that contributed by both dislocations and twins, and with further deformation the three mechanisms continuously compete against each other. Compared to the Slip + Twin + SB simulation, the Slip + SB model shows similar shear contributions of the dislocations and shear bands. The more pronounced contribution of shear banding predicted by the Slip + Twin + SB model suggests that the development of shear bands is facilitated by shear strain accumulation in the twinned structure [14,20]. We hence note that the distribu-

tion of localized strain predicted by the shear band model in the Copper-oriented crystal corresponds to the shear band development, whereas the localization predicted by the Slip + Twin model is caused by dislocation shear deformation. For the cube-textured material, the shear band simulations show that the shear rate contributed by shear banding increases at a later stage compared to the Copper-textured material, and shear banding starts to dominate over the other deformation mechanisms after a strain of 0.4 (Fig. 4b). The initially Goss-oriented crystal exhibits zero shear rates of shear banding during the whole deformation range studied (Fig. 4c). These observations indicate that the materials with initial orientations of cube and Goss are advantageous for preventing shear band development, which is consistent with an investigation on the effects of different texture components on the formability of aluminum alloys [50]. For the initially Brass-R-textured single crystal, the shear band simulations predict that the decrease in shear contribution from dislocations together with the increase in the shear rate contributed by shear banding occur at an early stage of deformation (below 0.1 strain as shown in Fig. 4d). This suggests that shear band systems are readily activated in this material at an early loading stage. However, further deformation

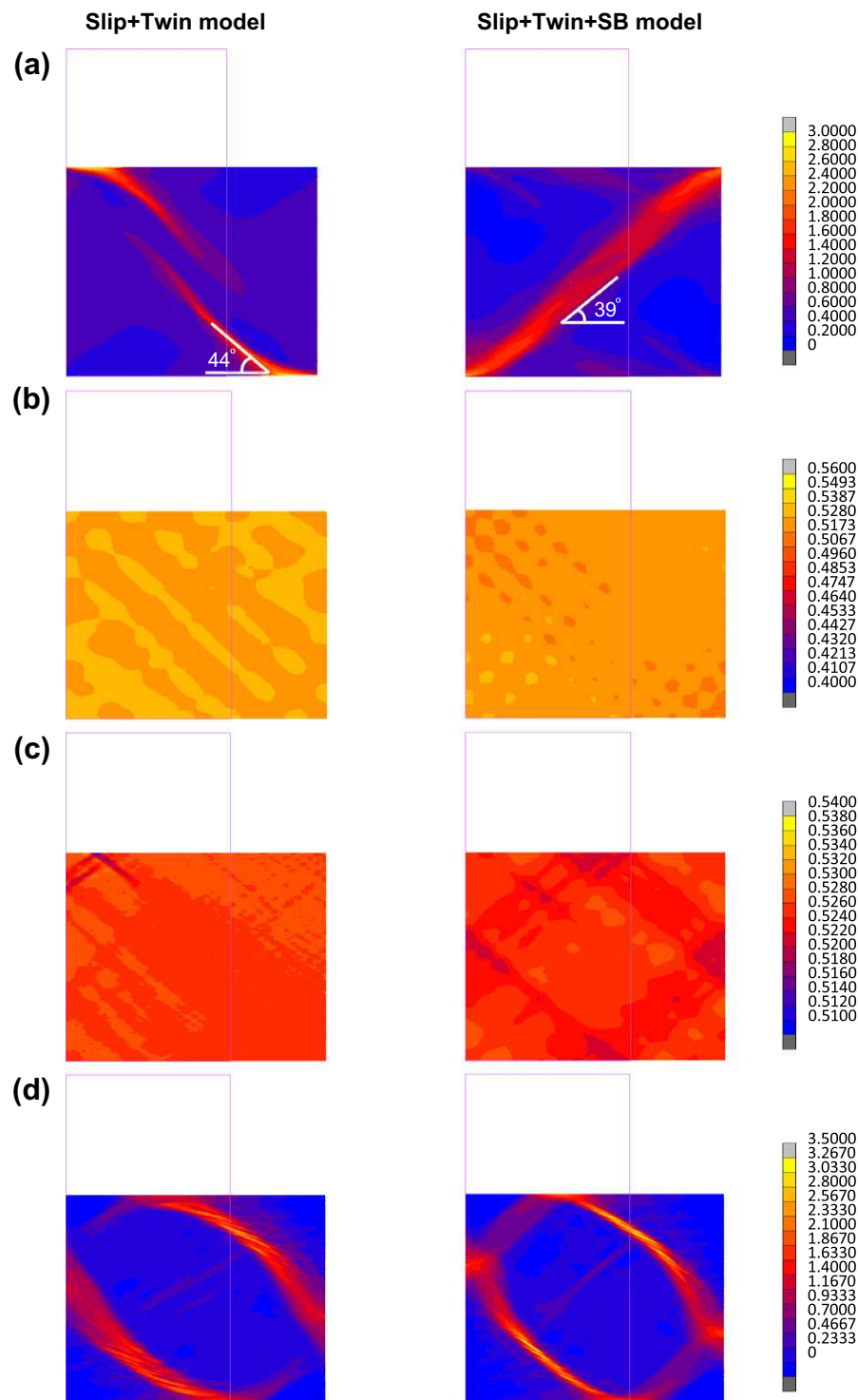


Fig. 3. Predicted distributions of equivalent logarithmic strain for single crystals with different initial orientations at 37% thickness reduction: (a) Copper, (b) cube, (c) Goss and (d) Brass-R. Left column: Slip + Twin simulations; right column: Slip + Twin + SB simulations. Red square frame indicates geometry of the undeformed crystal.

proceeds mainly via dislocation slip rather than via shear banding, although the shear contribution on shear bands has reached the maximum below 0.25 strain. It is also of interest to note that unlike the Copper-oriented crystal which exhibits a pronounced difference in strain pattern

between the Slip + Twin and Slip + Twin + SB simulations, the Brass-R material shows similar localization of strain in the two simulations except for some difference in magnitude of the localization and angle between the localization and ED. This is an indication that shear banding

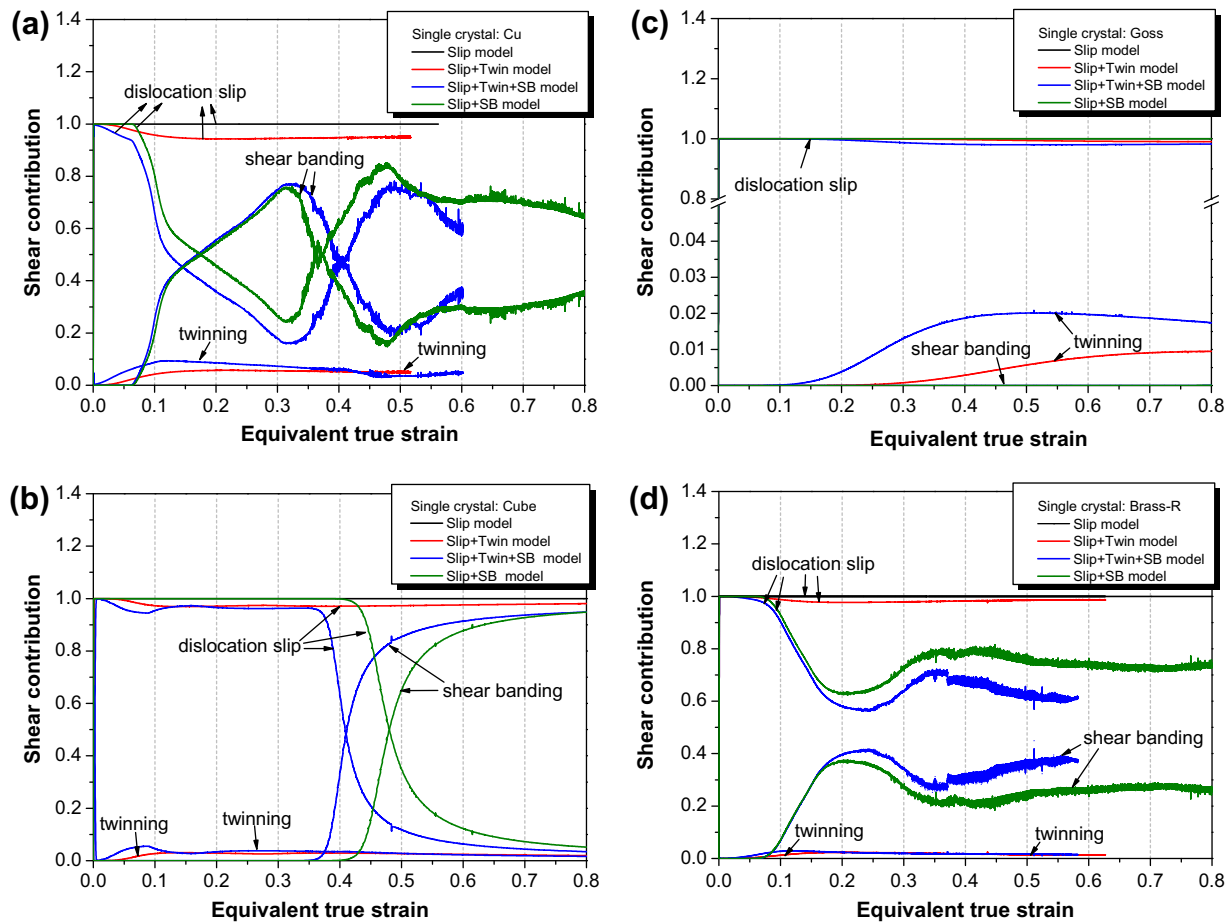


Fig. 4. Predicted shear contributed by the different deformation systems (dislocation slip, twinning and non-crystallographic shear banding) as a function of the equivalent true strain for single crystals with different initial orientations: (a) Copper, (b) cube, (c) Goss and (d) Brass-R.

activity is triggered at the material points where stress concentrations occur. However, this stress concentration does not necessarily occur in the regions with localized strain.

### 3.1.2. Crystallographic texture evolution

**3.1.2.1. Single crystal with initial Copper orientation.** With the aid of modern microtexture mapping techniques, i.e. transmission electron microscopy and electron back-scatter diffraction (EBSD), numerous studies on local orientation changes in fcc single crystals with low SFE have appeared in the past decade [8,13,14,19,40,51–54]. Among the many relevant texture components single crystals with Copper orientation were mostly selected for such studies owing to their tendency to form complex microstructures, specifically shear bands. It is an important advantage in corresponding experiments that the topological analysis of shear banding for crystals of this specific orientation by serial sectioning and three-dimensional EBSD methods can be omitted since the shear zones are formed on a plane parallel to TD [19]. Systematic measurements of local orientations have been performed on many Copper-textured materials, such as silver [8,14], Copper [8,19], and Cu–Al alloys [8,13,40]. In this section, the simulated local texture evolution of an initially Copper-oriented single crystal is

compared to the very well documented measurements conducted on a  $(112)[11\bar{1}]$  oriented Copper sample exposed to channel-die deformation at 77 K by Paul et al. [19]. In this work TEM orientation mapping was performed and pole figures of the differently deformed zones, i.e. of the matrix, matrix/shear band boundary and the shear band interior were individually displayed as shown in Fig. 5.<sup>1</sup> The ideal positions of the characteristic texture components developed during plane strain compression are shown in Fig. 5d. The strong primary matrix orientation components, i.e.  $(4411)[11\bar{1}\bar{1}\bar{8}]$  (D) and  $(26265)[\bar{5}\bar{5}52]$  ( $D^T$ ) are gradually weakened when moving from the matrix (Fig. 5a) towards the shear banding area (Fig. 5b). Inside the shear band they disappear (Fig. 5c). This process is characteristic of the orientation maps observed for many low SFE metals, although the texture intensity changes as the shear bands develop [8,13,14,40]. Within the well-developed shear band, a wide range of crystallographic orientations resulting from TD rotations of matrix regions are found, while the dominance of orientations near Goss

<sup>1</sup> Experiments were performed on the mixed microstructure with a well-developed shear band crossing twinned matrix in a 50% deformed sample, as shown in Fig. 8 of Ref. [19].



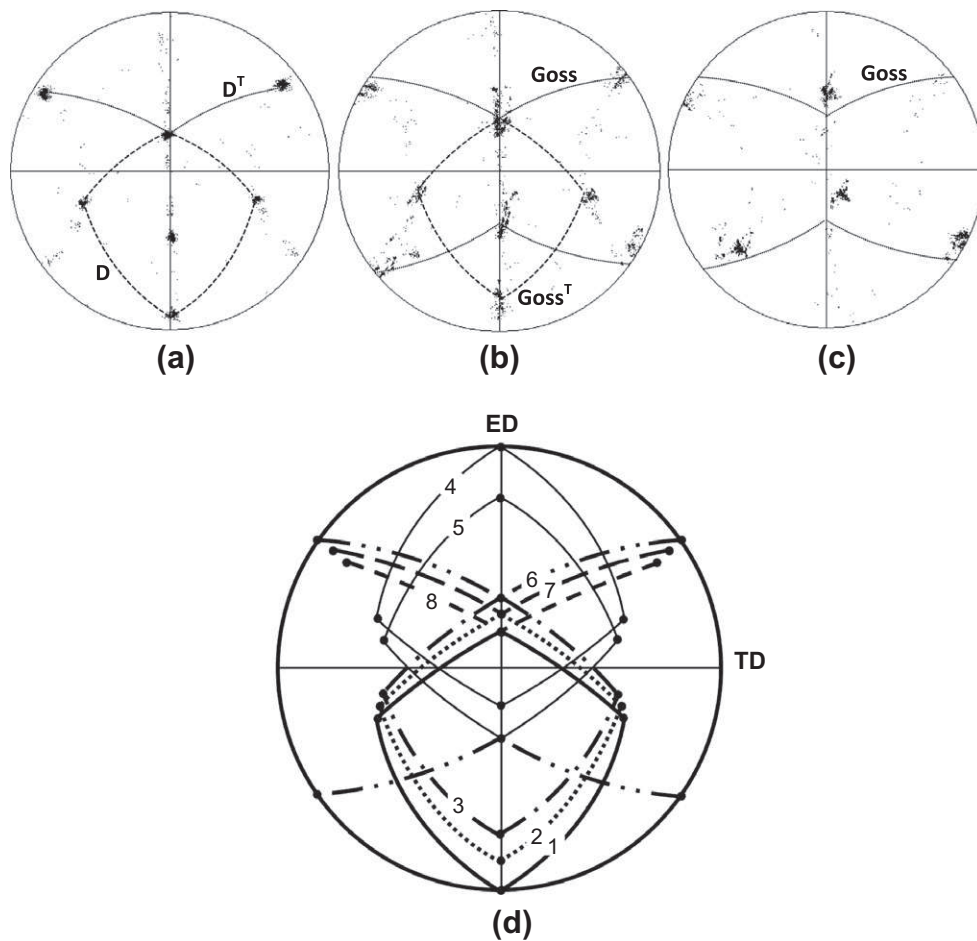


Fig. 5. Experimental  $\{111\}$  pole figures of different areas: (a) twinned matrix, (b) matrix/shear band boundary, and (c) shear band in a Copper orientated Copper after channel-die deformation at 77 K [19]. (d) Schematic sketch showing ideal positions of the characteristic texture components in a  $\{111\}$  pole Fig. 1:  $(112)[11\bar{1}]$ ; 2:  $(4411)[111\bar{8}]$ ; 3:  $(114)[22\bar{1}]$ ; 4:  $(112)[\bar{1}\bar{1}1]$ ; 5:  $(11,4)[\bar{2}\bar{2}1]$ ; 6:  $(110)[001]$ ; 7:  $(26265)[\bar{5}\bar{5}52]$ ; 8:  $(552)[\bar{1}\bar{1}5]$ . All these texture components develop from the  $(112)[11\bar{1}]$  orientation during plane strain compression.

and  $(114)[\bar{2}\bar{2}1]$  ( $\text{Goss}^T$ ) is evident (Fig. 5c). In the boundary (transition) area, orientation components both, from the twinned matrix and the shear bands are identified.

Fig. 6 shows the  $\{111\}$  pole figures of the Copper-orientated crystal after different thickness reductions as predicted by the Slip + Twin and Slip + Twin + SB models. The orientations extracted from the FE integration points with and without strain localization are used to calculate the crystallographic textures of the areas with strain localization and of the matrix, respectively. The orientations from all FE integration points represent the global textures of the sample. After 5% thickness reduction localization has not occurred at any integration point, thus only the global textures are presented. At this strain level, the initial orientation is essentially inherited in both cases. After 20% deformation, no obvious differences in orientation density are found among the two different types of areas by using the Slip + Twin model. The texture components in the matrix and within the strain localized zones include the Copper and the  $(552)[\bar{1}\bar{1}5]$  ( $\text{Copper}^T$ ) components. Weak D and  $D^T$  are also identified. Similar textures are obtained from the Slip + Twin + SB simulation except for the disap-

pearance of the initial Copper orientation in the strain localized area. After 37% reduction, differences between the two model predictions become evident. Using the Slip + Twin model, some orientation splitting about TD is predicted in the matrix area, while in the area with strain localization a transition from the Copper component towards the  $\text{Copper}^T$  and D components is clearly identified. As the strain localized area only covers a small fraction of the entire sample (Fig. 3a), the D component does not appear in the global texture. The experimental textures within the shear band area are apparently not of Copper-type as would be expected from homogeneous dislocation shear deformation. We hence suggest that shear banding is responsible for the inhomogeneous distribution of the textures in low SFE fcc materials. On the other hand, the Slip + Twin + SB model predicts that in the localization zones the D and  $D^T$  components decrease while Goss and  $\text{Goss}^T$  texture components increase significantly, while the textures in the matrix area remain stable, as is predicted by the model without shear banding. Still, by using the shear band model, a global texture evolution from  $\text{Copper}^T$ , D and  $D^T$  towards Goss and  $\text{Goss}^T$  is predicted.

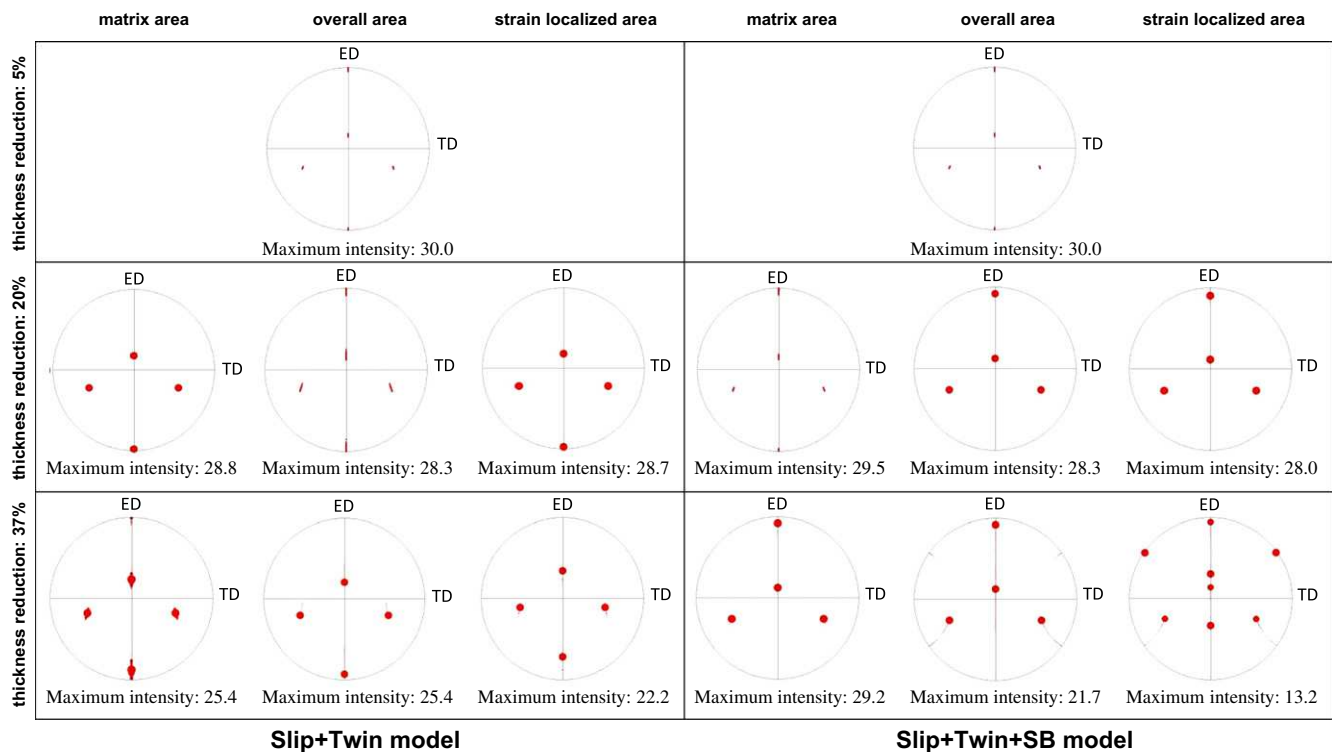


Fig. 6. Predicted {111} pole figures of different areas (matrix area, overall area and strain localized area) in the initially Copper-oriented single crystal at thickness reductions of 5%, 20% and 37%, respectively.

Comparing the simulations with the different deformation mechanism, it is revealed that the model incorporating non-crystallographic shear contributions captures the local orientations in the different areas more adequately when compared to the experiments.

**3.1.2.2. Single crystals with initial cube and Goss orientation.** As predicted by the Slip + Twin and Slip + Twin + SB simulations, the cube- and Goss-oriented crystals exhibit a homogeneous strain distribution at 37% and also at higher thickness reductions. This is in accordance with experimental observations that in fcc crystals with these initial orientations under plane strain load only a uniform dislocation-related microstructure evolves and no band-like strain localization occurs during plane strain deformation [53,54]. The current simulations also predict that perfectly oriented cube and Goss crystals remain quite stable up to 80% thickness reduction. Hence, we do not show the corresponding pole figures of these materials.

It is worth noting that the cube-oriented crystal in fcc metals is only metastable under plane strain loads, owing to the fact that the lattice rotation of the crystal sensitively depends on the exact initial orientation and the imposed boundary conditions [55–57,31]. In order to observe texture evolution of the cube orientation under the effect of shear banding, simulations on a sample with an initial orientation scatter prior to loading are performed [33,56,57]. More specific, the initial texture scatter of the near-single crystal sample is described in the form of a spherical Gauss

component [24,56] with a full width at half maximum of  $10^\circ$ , while the other simulation parameters are not changed [56]. Since the shear band systems in the cube-oriented crystal are activated at a later deformation stage compared to the Copper and Brass-R orientations, the simulation results up to 80% deformation are presented for the initially textured material. As predicted by both simulations (i.e. with and without shear banding model) (Fig. 7), after 40% thickness reduction orientation splitting about both, ED and TD become evident [56]. After 80% thickness reduction, both models exhibit a clear texture transition from cube towards Goss. However, the shear band simulation shows that the orientation splitting about the ED is impeded with the initiation of the shear band systems.

**3.1.2.3. Single crystal with initial Brass-R orientation.** Fig. 8 shows the texture evolution of the Brass-R-oriented crystal obtained from the Slip + Twin and Slip + Twin + SB simulations. Both models show that at 5% thickness reduction when no strain localization occurs anywhere in the material, the global texture is dominated by the Brass-R component. After 20% deformation, the Slip + Twin model does not show substantial texture changes in either the matrix or the strain localized areas except for a minor deviation from the original orientation. After 37% deformation in the matrix area the Copper and  $(113)[33\bar{2}]$  (close to the D orientation) components are developed. In the strain localized area a development of the  $(113)[33\bar{2}]$  and  $(221)[\bar{1}\bar{1}4]$  (close to the Copper<sup>T</sup> orientation) components is predicted, accompanied by a complete reduction of the

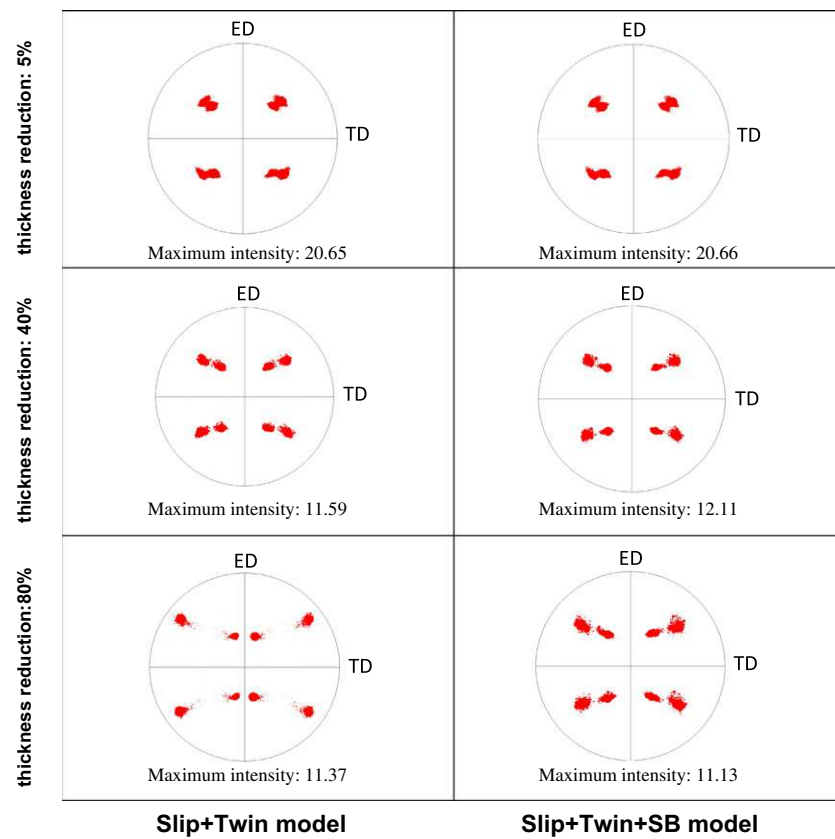


Fig. 7. Predicted  $\{111\}$  pole figures of the initially cube-oriented single crystal with a  $10^\circ$  spherical Gaussian orientation scatter about this ideal texture component at thickness reductions of 5%, 40% and 80%, respectively.

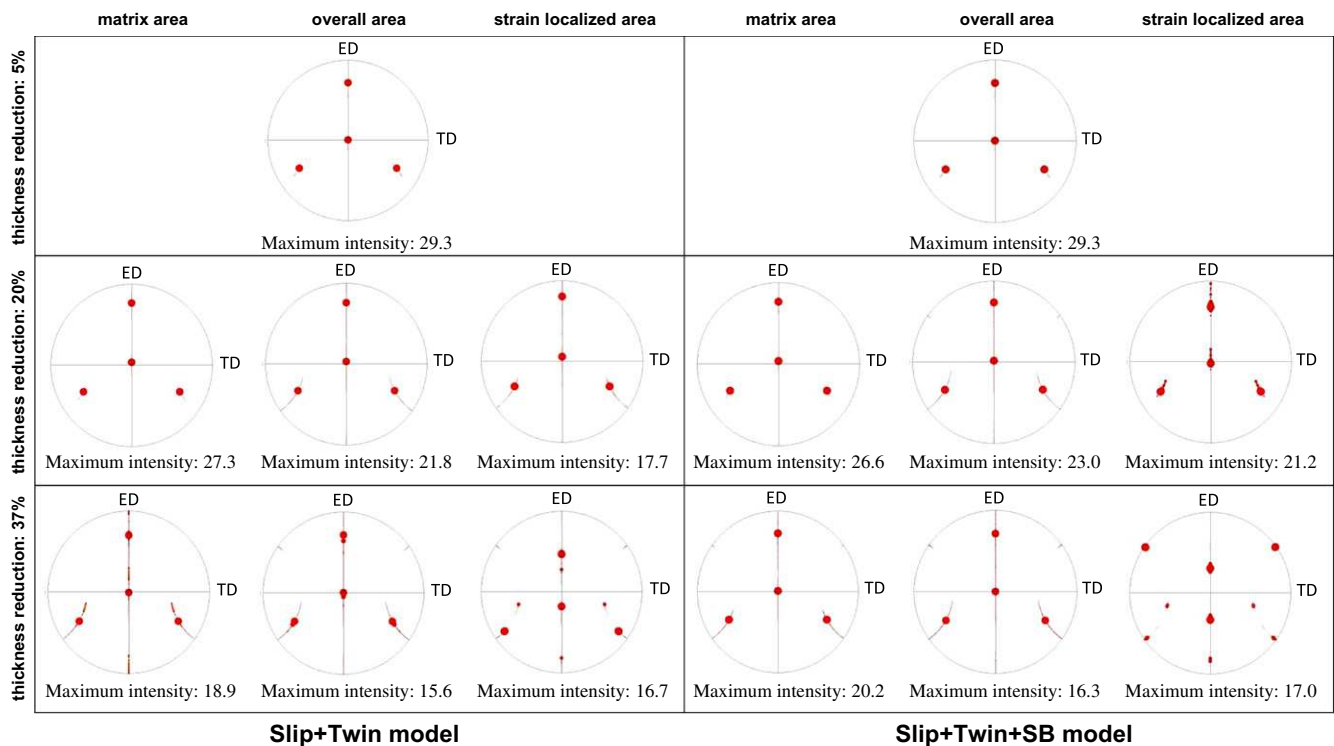


Fig. 8. Predicted  $\{111\}$  pole figures of different areas (matrix area, overall area and strain localized area) in the initially Brass-R-oriented single crystal at thickness reductions of 5%, 20% and 37%, respectively.

Brass-R component. The Slip + Twin + SB simulation predicts that at 20% deformation in the strain localized area the original Brass-R orientation is shifted towards the Copper and  $(113)[33\bar{2}]$  components, while the textures in the matrix area only show a minor change. When using the shear band model, after 37% deformation a significant development of the Goss and Goss<sup>T</sup> components is predicted in the shear band zones. The  $(221)[\bar{1}\bar{1}4]$ ,  $(113)[33\bar{2}]$ , and  $(14143)[\bar{3}\bar{3}28]$  (close to the D<sup>T</sup> orientation) components are also predicted in this area. At this stage the Brass-R component has been reduced in the strain localized area; however, it remains stable in the matrix. According to both simulations, as the overall fraction of the zones that are affected by localization is small (Fig. 3d), the global texture components resemble those in the matrix area.

### 3.2. Group 2 (Copper-oriented single crystal with same boundary conditions but different specimen aspect ratio)

Using the Slip + Twin + SB model, the group 2 results on the strain distribution and shear rate of the shear band systems after 20% thickness reduction are shown in Fig. 9. At that strain level, zones with localized strain appear in all simulations (Fig. 9a). For the crystals with low aspect ratios (0.5 and 0.67), less significant and broader localization with a width of  $\sim 20$  elements is predicted. In the case of higher aspect ratios (1.0 and 2.0), very sharp localization with a width below five elements is predicted. The initiation of the shear band systems that correspond to the strain localized zones is also identified in all the crystals (Fig. 9b). It is noted that the formation of shear bands depends on the thickness-to-length ratio of the modeled

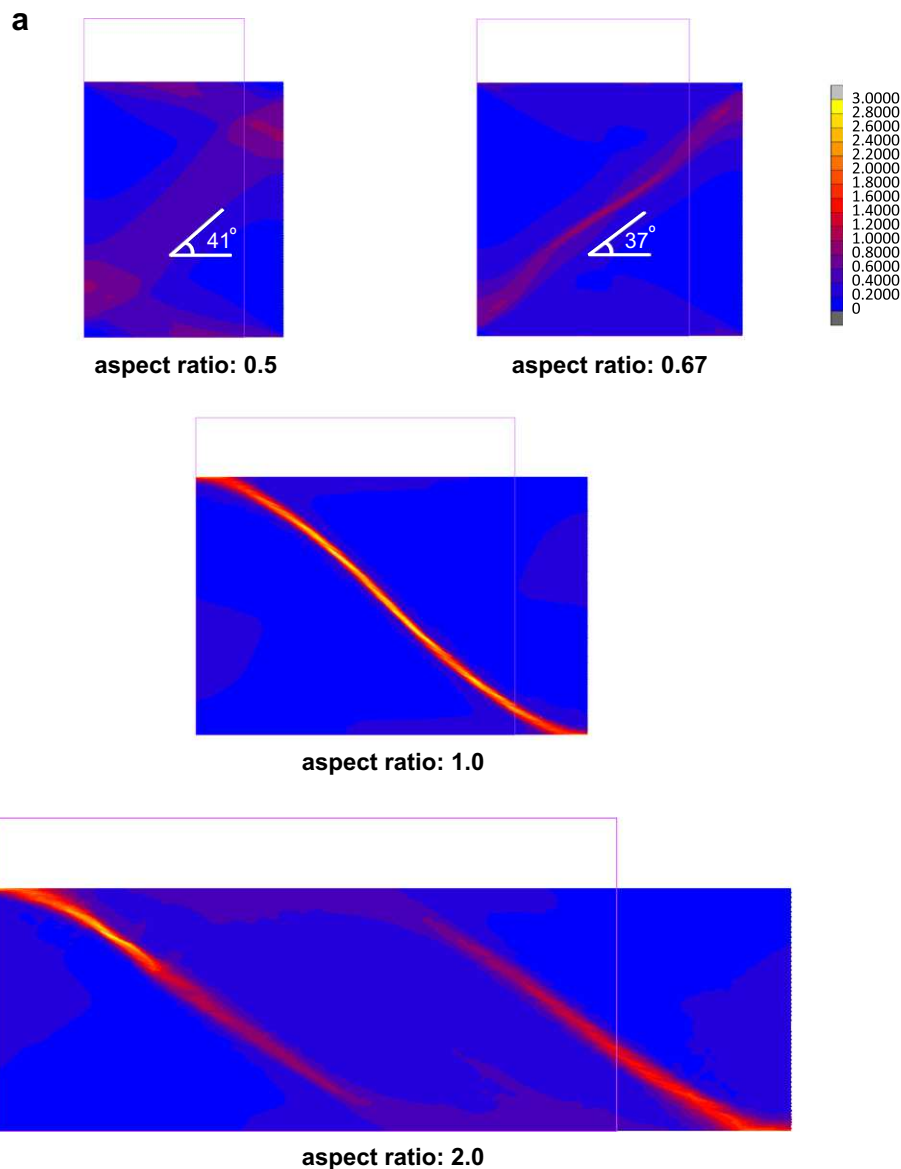


Fig. 9. Predicted distributions of (a) equivalent logarithmic strain and (b) shear rate of the shear band systems for the initially Copper-oriented single crystal with different aspect ratio (0.5, 0.67, 1.0 and 2.0) at 20% thickness reduction. These simulations used the Slip + Twin + SB constitutive models.



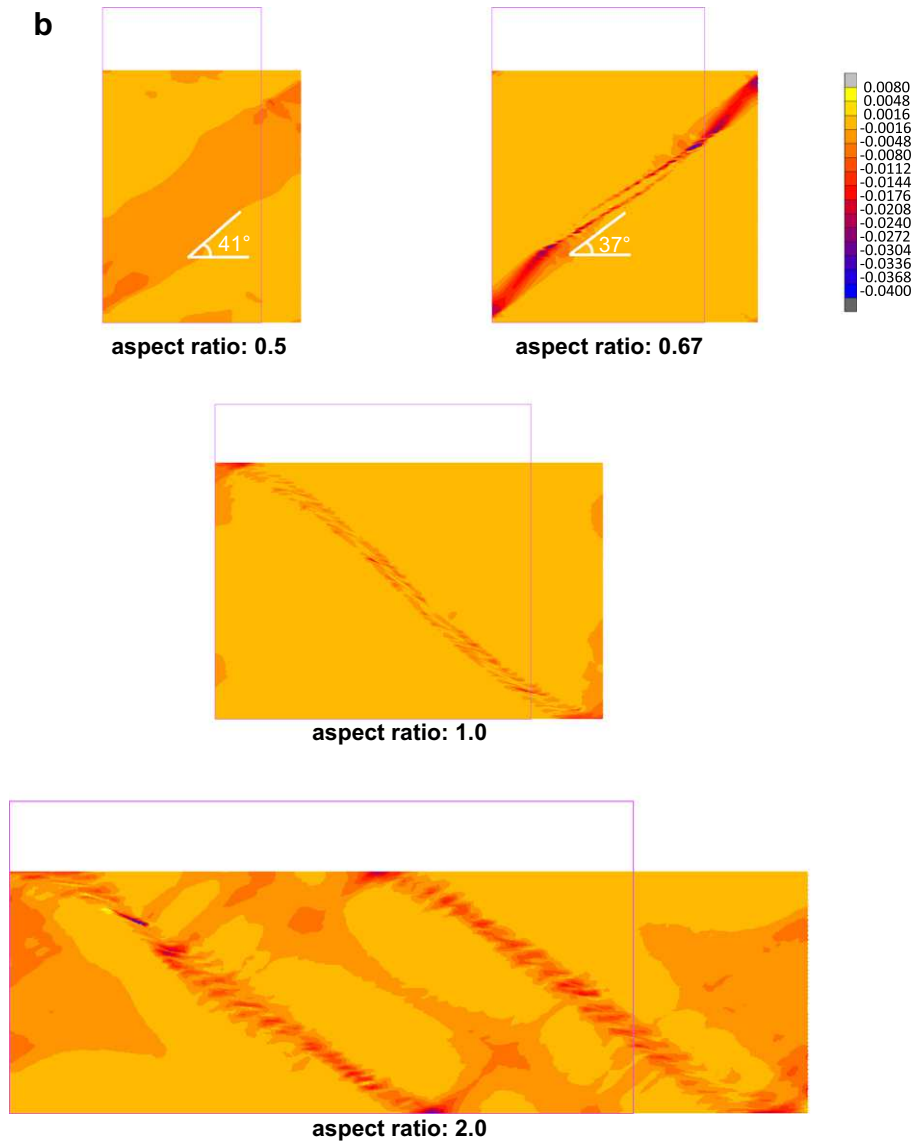


Fig 9. (continued)

sample. The crystal with an aspect ratio of 0.5 shows a  $41^\circ$  inclination of the shear band relative to ED, while the crystal with an aspect ratio of 0.67 shows a smaller inclination angle of  $37^\circ$ . In addition, the simulations with lower aspect ratios show shear bands in the direction between the left and right bounding edges (bottom-left and top-right), whereas the high aspect ratio simulations show shear bands in the other directions between the top and bottom edges. To identify the individual contributions of dislocation slip, twinning and shear banding to the overall deformation, the evolution of the normalized shear rates on the different deformation systems is presented in Fig. 10. All simulations indicate that the shear band systems are activated at an early stage of deformation. However, at 20% deformation (0.22 strain), the models which assumed aspect ratios of 0.5 and 0.67 predict a more pronounced contribution of shear bands to the overall deformation compared to the predictions obtained for aspect ratios 1.0 and 2.0. This

means that the origin of the strong strain localization as predicted by all simulations is different for the low and high aspect ratio models. In this context, the question arises why the different models predict a different distribution of shear bands. The possibility that a smaller thickness-to-length ratio of the sample induces a shape instability, can be ruled out because for the simulated crystals in this study even the smallest aspect ratio of 0.5 is much larger than the critical ratio at which geometrical softening occurs [58].

### 3.3. Group 3 (Copper-oriented single crystal with same aspect ratio but different boundary conditions)

The focus here is on the boundary-condition-dependent shear banding of single crystals under plane strain compression. For this parameter study we deform a Copper-oriented crystal as it has a high tendency to initiate shear

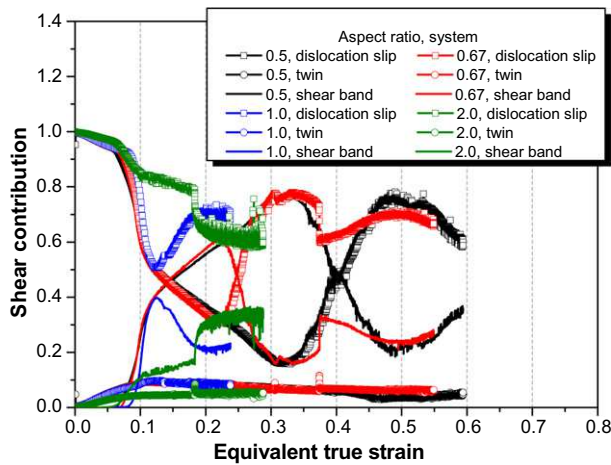


Fig. 10. Predicted shear contributed by the different deformation systems (dislocation slip, twinning and shear banding) as a function of equivalent true strain for the initially Copper-oriented single crystal with different aspect ratio (0.5, 0.67, 1.0 and 2.0). These simulations used the Slip + Twin + SB constitutive models.

bands. Fig. 11 shows the distribution of the equivalent logarithmic strain, the shear rate of the shear band systems as well as the equivalent Cauchy stress obtained from simula-

tions with specific boundary conditions “Tie Right”, “Relax Right”, “Relax Both”, and “PBC” (as explained in Section 2.3). Different color coding is used to show the magnitude of the variables for the respective simulations. It is revealed that at 20% thickness reduction (Fig. 11a), the accumulated strain is localized close to the top and bottom edges of the samples in all cases and close to the left and right bounding edges in the “Tie Right” case. In the simulations with “Relax Right” and “Relax Both” boundary conditions, significant curvature of the edges perpendicular to ED appears. Accordingly, strong strain localization related to mesh distortion near the left and right edges is observed in these cases. A clear initiation of the shear band systems associated with free edge curvature is also predicted in Fig. 11b, which is consistent with the distributions of strain and stress. More specific, zones with a high shear rate contribution from shear bands also exhibit a clear localization of the equivalent logarithmic strain. The activation of the shear band systems is triggered by the stress concentration in the shear banding zones (Fig. 11c). The results at a higher thickness reduction predicted by the simulations with “Tie Right” and “PBC” boundary conditions are presented in Fig. 12 (convergence is obtained in these simulations). For the simulation with “Tie Right”

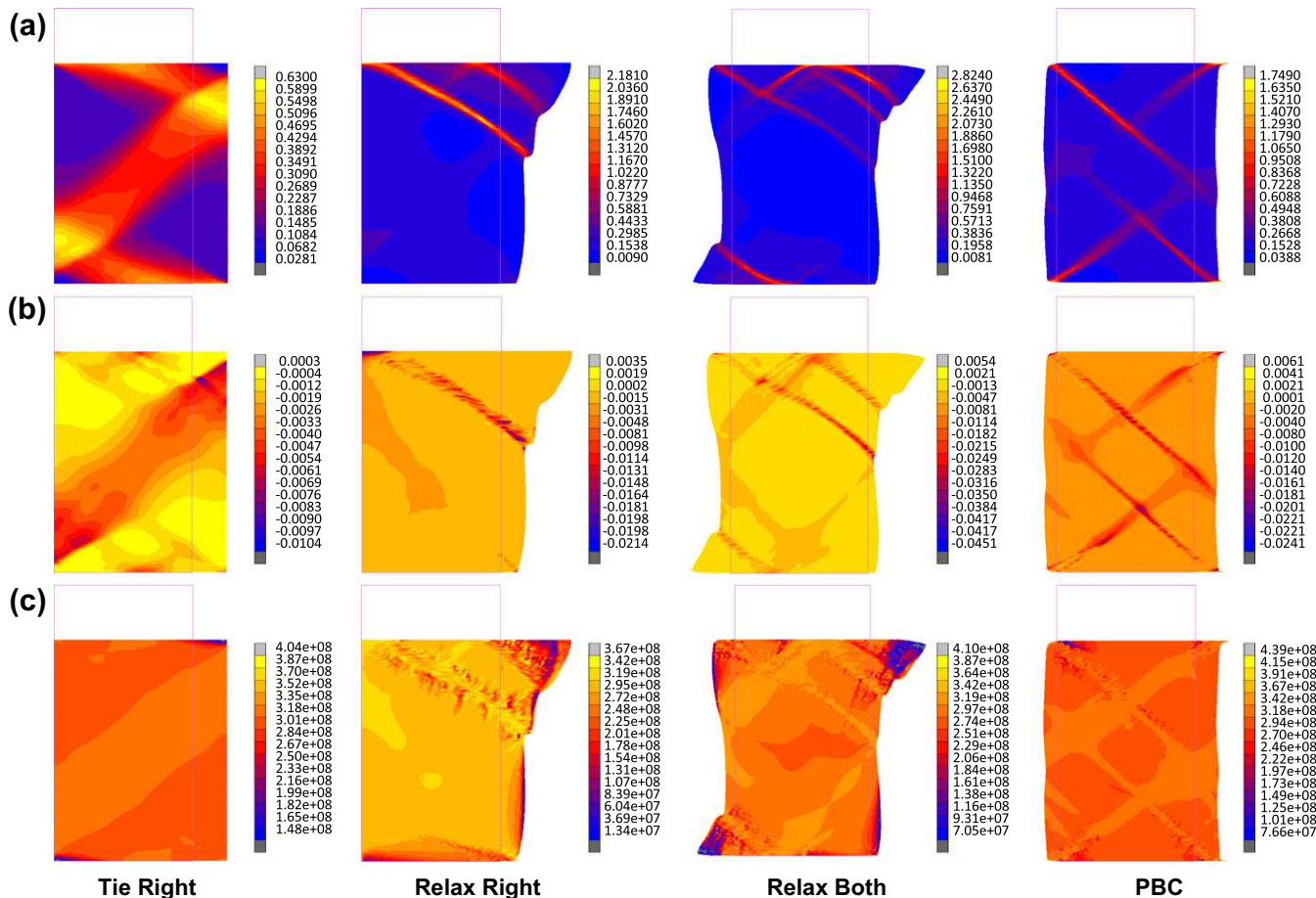


Fig. 11. Predicted distributions of (a) equivalent logarithmic strain, (b) shear rate of the shear band systems and (c) equivalent Cauchy stress for the initially Copper-oriented single crystal with different boundary conditions (“Tie Right”, “Relax Right”, “Relax Both”, and “PBC”) at 20% thickness reduction. These simulations used the Slip + Twin + SB constitutive models.

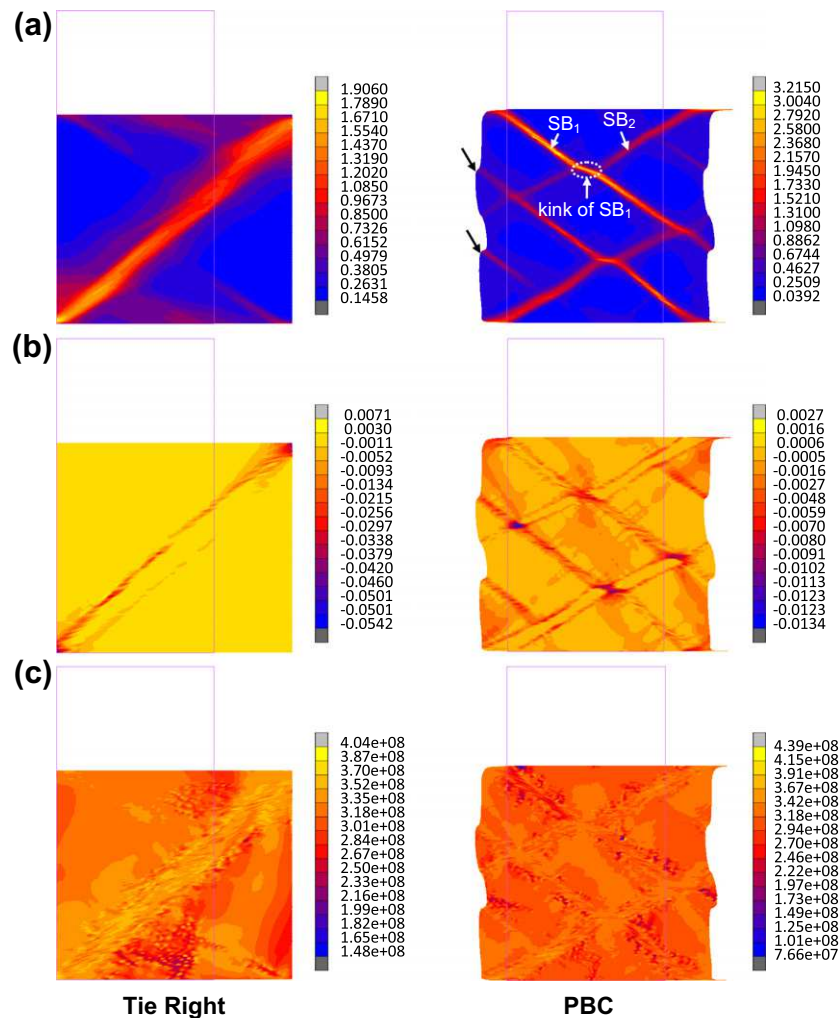


Fig. 12. Predicted distributions of (a) equivalent logarithmic strain, (b) shear rate of the shear band systems and (c) equivalent Cauchy stress for the initially Copper-oriented single crystal with different boundary conditions (“Tie Right” and “PBC”) at 32% thickness reduction. These simulations used the Slip + Twin + SB constitutive models. Jogs on the free edges and kink of the first family of shear bands ( $SB_1$ ) are indicated in the simulation using “PBC” boundary conditions.

boundary conditions, a pronounced shear band forms between the left and right edges. The results for the simulation with “PBC” boundary conditions also show very severe shear bands with significant strain localization. With the same color coding as that used for 20% reduction, the stress contours show a more homogeneous distribution throughout the sample. This indicates a release of stress inside the shear bands. Moreover, activation of the shear band systems is localized at the border of the bands, suggesting that shear banding starts to accommodate the imposed deformation between shear bands and zones outside the bands. Another important characteristic of the simulations is that the shear within the bands leads to jogs on the free edges (black arrows in Fig. 12), as also predicted by the simulation using “Relax Both” boundary conditions at 20% deformation (Fig. 11). This agrees very well with experimental observations on low SFE fcc crystals with a structure saturated with macroscopic shear bands [8,14,19].

## 4. Discussion

### 4.1. Orientation dependence of shear banding (Group 1)

In the developed shear band model, the potential shear band systems are activated when a critical resolved stress, i.e. a resistance to shear banding, is reached at a material point. Consequently, the effect of the initial orientation on shear band formation is due to the mechanical properties of the individual crystals. More specific, the difference in the mechanical properties between the different orientations is related to the critical shear stress relationship among the competing deformation modes and their orientation-dependent activation. To show this more clearly, the equivalent true stress–equivalent true strain curves of the orientations obtained from the Slip + Twin simulations are shown in Fig. 13, indicating different yielding and strain-hardening behaviors of the crystals deformed via dislocation slip and twinning. The crystal that requires a

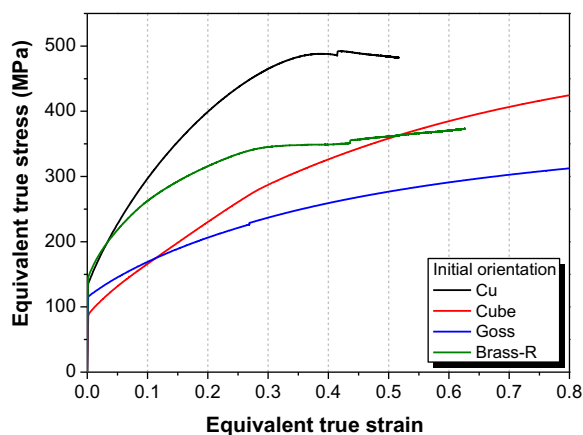


Fig. 13. Predicted equivalent true stress-equivalent true strain responses of the differently orientated single crystals by using the Slip + Twin constitutive models.

higher stress for deformation yields earlier localization and hence shear band formation. For instance already at a strain level below  $\sim 0.4$  the Copper-oriented crystal shows the highest stress and the strongest tendency to form shear bands, whereas the Goss-oriented crystal shows the lowest flow stress and yields a homogeneous strain distribution. For the set of representative single crystal orientations included in the present study, the tendency to initiate shear banding increases in the order: Goss, cube, Brass-R, Copper. The shape and stability of the flow curves in Fig. 13 is analyzed in terms of the Considère instability criterion, i.e. in terms of the point at which  $d\sigma/d\varepsilon = \sigma$  is satisfied. This relation identifies the point where further strain hardening becomes insufficient to compensate for geometrical softening. The intersection between the stress-strain curve and its derivative occurs at  $\varepsilon = 0.3$  for the Copper orientation, 0.43 for the cube orientation, 0.35 for the Goss orientation, and 0.25 for the Brass-R orientation, respectively. This exactly reflects the tendency of shear band initiation in the differently oriented crystals. More specific, the Copper and Brass-R orientations are less stable and experience more geometrical softening compared to the cube and Goss orientations. The result is consistent with the predictions by the Slip + Twin + SB model, namely, that the Copper and Brass-R-textured materials exhibit much earlier increase of the shear rates on the shear band systems than the cube and Goss-oriented crystals.

According to the investigation of Al–Mg crystals [18], shear bands are found in Copper-oriented crystals, but not in Goss crystals. The authors suggest that the initially Copper-oriented crystals exhibit an asymmetry of the active slip systems, which contributes to the formation of a lamellar dislocation structure parallel to prevalent slip plane. For this reason shear banding is initiated preferentially in Copper-oriented grains. In agreement with the explanation, a more homogeneous dislocation structure without shear bands is developed in the Goss orientation with a more symmetrical arrangement of the slip systems. Regarding this trend, our predicted orientation dependence

of shear banding is consistent with the microstructure-dependent activity of the slip systems as reported in the literature [18].

#### 4.2. Effects of shear banding on texture evolution (Group 1)

The simulations using the shear band constitutive model predict significant non-crystallographic shear banding in the Copper, Brass-R and cube-oriented crystals at strain levels above 0.07, 0.1 and 0.4, respectively (Fig. 4). For the crystals initially oriented with Copper and Brass-R, the texture components inside the shear bands have rotated towards Goss after 37% thickness reduction. For the cube crystal with an initial orientation scatter of  $10^\circ$ , this texture transition is predicted by both the Slip + Twin and Slip + Twin + SB models, although the orientation seems to be more stable against reorientation with the initiation of shear banding.

As most of the experimental observations on shear banding are available for deformed Copper-oriented single crystals, we focus the following discussion on this orientation. According to the experimental results on Copper-oriented fcc single crystals by Paul et al. [8,19], at small plastic strains the crystals deform by homogeneous slip on four slip systems with identical Schmid factor. Two of them operate as co-planar (CP) systems while the others are co-directional (CD). This slip activity is well reproduced by both the Slip + Twin and Slip + Twin + SB simulations showing an angle of  $19.5^\circ$  and  $35.3^\circ$  between the slip planes and the ED, respectively. More specific, the initial deformation stage mainly proceeds on the  $(111)[0\bar{1}1]$  and  $(111)[\bar{1}01]$  pair of CP slip systems together with the  $(\bar{1}\bar{1}1)[110]$  and  $(1\bar{1}1)[110]$  pair of CD slip systems. The simulations also predict that dislocation slip leads to a  $\sim 8^\circ$  lattice rotation about TD from the initial Copper component towards the D component, and twinning transforms the matrix orientations from D and Copper into the  $D^T$  and  $Copper^T$  orientations. This result is in accordance with the experiments [8,19]. With increasing strain, the Slip + TwinSlip + Twin model shows that the crystal still deforms by dislocation slip on the above-mentioned CP and CD systems and by twinning. However, the Slip + Twin + SB model predicts that as strain reaches  $\sim 0.07$ , dislocation slip on both, the CP and the CD slip system pairs sharply drops and shear banding starts to prevail. At a strain above  $\sim 0.3$ , the shear rate on the shear band systems decreases with deformation, while the above-mentioned CP systems and a second pair of CP systems ( $(\bar{1}\bar{1}1)[011]$  and  $(\bar{1}\bar{1}1)[101]$ ) become more active. The new slip systems are found to operate in the strain localized area, implying an increase of the Schmid factor on the reoriented  $(\bar{1}\bar{1}1)$  plane. With the texture transition inside the area towards the Goss and  $Goss^T$  components, the CP systems contribute even more shear. Inside the shear bands the orientations D (of the primary matrix) and  $D^T$  (of the twin) must undergo a  $\sim 8^\circ$  rotation around the  $\langle 110 \rangle$  axis to reach the Goss and  $Goss^T$  orientations,



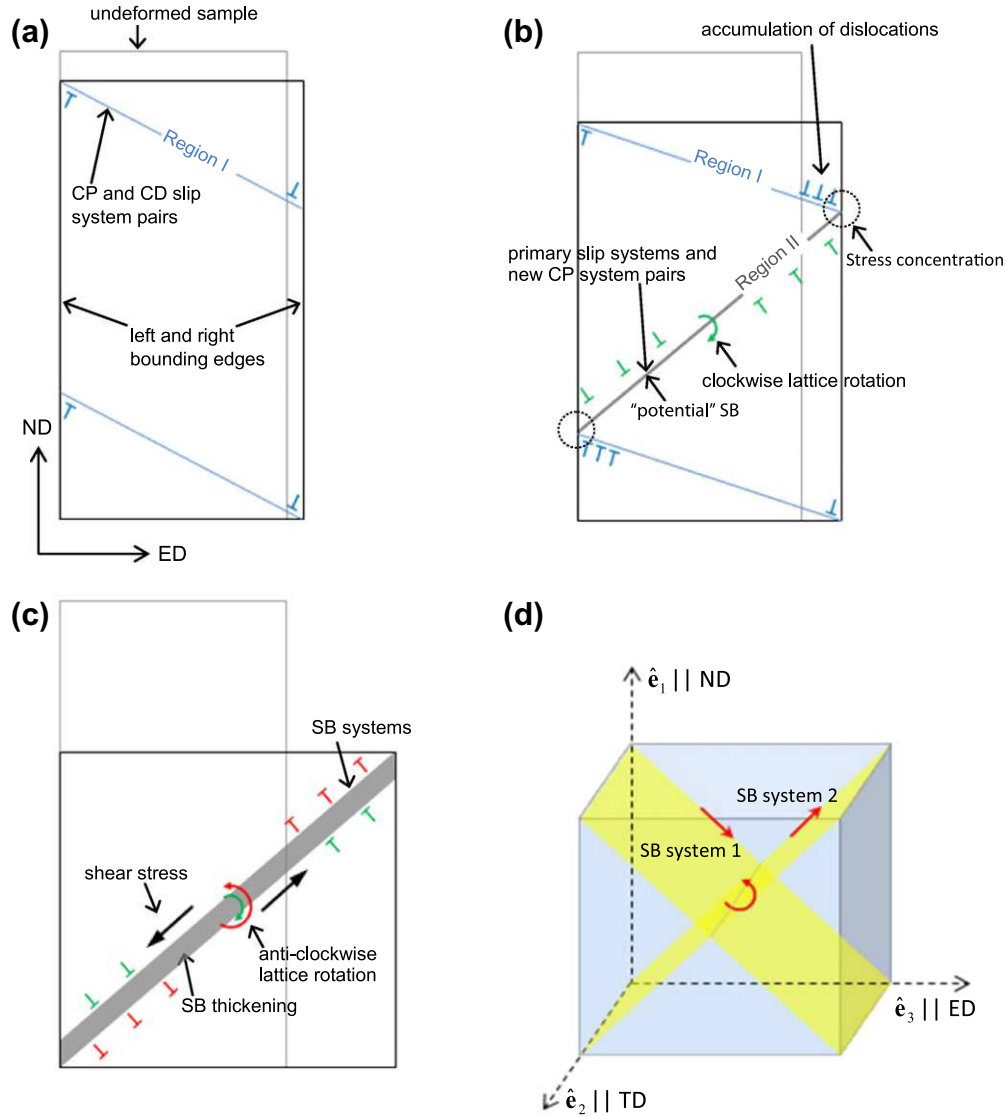


Fig. 14. Schematic presentation of the successive stages of plane strain compression for a sample with an aspect ratio of 0.5 and boundary conditions “Tie Right”: (a) strain localization induced by dislocation activity on the CP and CD slip system pairs, (b) dislocation accumulation at the hard bounding edges leading to an activation of the new CP system pair between the edges and to a “potential” shear band, (c) activation of the shear band systems together with dislocation slip along shear band plane leading to local lattice rotation. (d) Schematic of lattice rotation induced by shear banding on a pair of ( $\hat{e}_1$ – $\hat{e}_3$ )-shear band planes. The rotation axis is parallel to the shear band planes. CP: co-planar, CD: co-directional, ED: elongation direction, ND: normal direction, TD: transverse direction, SB: shear band.

respectively. This rotation is suggested to occur when the  $(111)[0\bar{1}1]$  and  $(111)[\bar{1}01]$  slip systems are equally activated, following which shear banding would be facilitated by crystallographic slip on the resultant system  $(111)[\bar{1}\bar{1}2]$  [19]. However, the operation of the  $(111)$  CP systems is not sufficient to shift the textures towards Goss and Goss<sup>T</sup>, according to our Slip + Twin simulation (Fig. 6). In the case of the Slip + Twin + SB simulation, the non-crystallographic shear contribution in addition to dislocation and twinning shear is considered. The principal stresses that matter for the constitutive shear band law are derived by principal axis transformation from the second Piola–Krichhoff stress tensor. By ordering these principal stresses according to  $|\sigma_1| \geq |\sigma_2| \geq |\sigma_3|$  with  $\sigma_1 \leq 0$ ,  $\sigma_2 \leq 0$ ,  $\sigma_3 \geq 0$  (cf. Eq. (10)), the shear stress in the plane

constructed by the two orthonormal principal directions  $\hat{e}_1$  and  $\hat{e}_3$  (corresponding to the maximum compression stress and the tensile stress) is known to mostly promote shear banding. Then, in the strain localized area where shear banding has been initiated, significant deformation in the two ( $\hat{e}_1$ – $\hat{e}_3$ )-shear band planes imposes an additional rotation around the TD ( $\parallel \langle 110 \rangle$ ) axis. As predicted by the shear band model, this lattice rotation then leads to the development of the Goss and Goss<sup>T</sup> components within the shear bands. Consistent results are found in the Brass-R-oriented single crystal, showing a significant texture transition from the initial and/or intermediate components to the Goss and Goss<sup>T</sup> components. For the cube crystal with an initial orientation scatter of  $10^\circ$  about the ideal component, this shear-band-induced lattice rotation

seems to disturb the dislocation-slip-related ED rotation, which explains the smaller orientation splitting about the ED axis compared to that obtained from the Slip + Twin simulation (Fig. 7).

#### 4.3. Influence of boundary conditions on the development of shear bands (Groups 2, 3)

For the Copper-oriented single crystal, simulations with different sample geometries predict different shear banding patterns. From the distribution of the shear bands (Figs. 9 and 10), it is found that the low aspect ratio models predict a more pronounced contribution by shear banding to the overall shear compared to that in the high aspect ratio models. On the other hand, the development of shear bands is linked to the hard boundaries (i.e. the left and/or right bounding edges perpendicular to ED), as predicted by the simulations with same sample geometry but different boundary conditions (Figs. 11 and 12). It should be mentioned that imposing hard boundary conditions on the crystal edges introduces a similar effect as the presence of twin boundaries, i.e. it provides barriers to dislocation motion. Then, based on the shear banding scheme proposed by Dorner et al. [9] for a bcc metal comprising groups of microbands in the deformation microstructure, a detailed analysis on how shear bands propagate across a single crystal and cause local lattice rotation in the current shear band simulations is suggested. Successive stages of the shear banding process for a sample with an aspect ratio of 0.5 and boundary conditions “Tie Right” are presented in Fig. 14a–d. At the initial stage, strain localization occurs in region I due to extensive dislocation activity on four slip systems, i.e. the CP and CD slip system pairs (Fig. 14a). Since the Copper orientation rotates to the D orientation at small strains, slip traces of the CP and CD systems form an angle of  $27.4^\circ$  to ED. One should note that in the low aspect ratio sample analyzed here, slip traces could reach the left and right bounding edges, which is different from the case of high aspect ratio models. Then, the localized strain induces dislocation accumulation at those boundaries. This is indicated by jogs on the free edges of a sample as predicted by the simulation using the same sample geometry but “Relax Both” boundary conditions. Because of the micro-mechanical interactions among the slip systems, dislocation activity in region I becomes difficult and dislocation slip on the primary slip systems also takes place in region II between the bounding edges (in Fig. 14b). With further straining and the accompanying lattice rotation in this region, another pair of CP systems on the  $(\bar{1}\bar{1}1)$  plane is activated. Moreover, stress concentration on the bounding edges is caused by the blockage of the edges to dislocation penetration. The stress field triggers activation of the shear band systems in the adjacent areas and leads to strain localization within region II where a shear band is formed potentially. At higher deformations, the shear band systems are continuously activated along the shear band planes, while slip on the  $\{111\}\langle 110 \rangle$  sys-

tems is facilitated again along those planes. This process induces local lattice re-orientation within the band (Fig. 14c). In our simulations without shear banding, dislocations on the primary slip systems pile up at the bounding edges, which causes the strain localized region between the edges to rotate clockwise. Therefore, both the slip and Slip + Twin constitutive simulations show that the initial orientation of Copper undergoes a negative rotation around TD towards the D component. For the shear band simulations in which dislocation blockage by the twin-matrix lamellar structure has occurred (e.g. the model with an aspect ratio of 0.5 and “Tie Right” boundary conditions), the activation of the shear band systems enables a lattice to be rotated anti-clockwise. More specifically, the region with localization undergoes a positive rotation around TD that is parallel to the most active shear band planes (Fig. 14d). Region II then undergoes two rotations and the net rotation is ultimately determined by the more favorable deformation systems. This explains why the non-crystallographic shear banding mechanism incorporated in the simulations leads to a positive lattice rotation about TD from the Copper component to the Goss component. The presented simulations also show that shear bands are inclined at  $30\text{--}45^\circ$  to ED. All these results are in accordance with the experimental observation that the crystallographic rotation inside the bands renders the  $(111)$  planes parallel to the shear plane [14,40]. This position then facilitates further strain accommodation by homogeneous slip along the shear plane. Consequently, the area outside the shear bands is gradually incorporated into the bands with further straining. This feature has also been extensively reported in the development of shear bands by experiments [14,20,40] and appears as band thickening in our simulations (compare Fig. 12 to Fig. 11). According to the current modeling on the Copper-oriented single crystal, shear banding starts to dominate over dislocation slip and twinning at a thickness reduction of 14% (0.15 strain). This means that in a microstructure with well-developed shear bands (above 0.3 strain), overall strain accommodation and compatibility at the bulk crystal or sample scale could actually be promoted by lattice reorientation and highly localized strain within shear bands. At higher deformations, a second family of shear bands ( $SB_2$ ) arranged roughly symmetrically to the first one ( $SB_1$ ) could be predicted with decreasing band inclination angle (Fig. 12). Then, the lattice rotation within the intersection zones of the two families of shear bands (the characteristic kinks of the first family), together with the subsequent shear along both families, accommodates the strain of the overall sample. As confirmed by experiments [13], the thickness of a band and its inclination with respect to ED determine the deformation contribution due to shear banding. The simulation results presented above explain mesoscopic structure development in the Copper-oriented crystal when shear bands propagate across the sample, which also agrees with observations of compressed Copper at 77 K [8,19] and silver [14] with Copper orientation.

## 5. Conclusions

We have presented crystal plasticity finite element simulations of the structure and texture developments in plane strain compressed  $\alpha$ -Brass single crystal samples with different characteristic initial orientations. By performing simulations incorporating different deformation mechanisms for each sample, especially for Copper-oriented crystals which are extensively studied in experiments in the literature, comparisons of simulated and experimental phenomena related to shear banding are evaluated. Simulations are then performed on Copper orientation with varying sample geometry and boundary conditions in order to reveal the underlying micromechanics of shear band deformation and its dependence on loading constraints. The main results are as follows:

- Initiation of shear banding depends on the initial orientation of crystals and their respective mechanical properties. For the studied single crystals, the tendency to form shear bands increases in the order: Goss, cube, Brass-R, Copper.
- Shear banding leads to inhomogeneous texture distribution in Copper and Brass-R-oriented crystals. For an initially Copper-oriented crystal, at small reductions, the shear band simulation shows that textures in the bulk matrix include Copper, Copper<sup>T</sup>, D and D<sup>T</sup> components. Similar textures are developed in the shear band area except for a disappearance of the initial orientation. At 37% deformation, a significant increase in the Goss and Goss<sup>T</sup> components is predicted inside the shear bands, while textures in the bulk crystal matrix remain stable. The simulated local texture evolution captures the major aspects of the experimental characterization for a Copper single crystal sample deformed at 77 K.
- Different shear banding behaviors are predicted for the Copper-oriented crystal with same boundary conditions (“Tie Right”) but different sample geometry. As the ratio of thickness to length is decreased, more pronounced contribution by shear banding to the overall shear is obtained. The simulated result is an indication that shear banding initiation is determined by the dislocation activity in actual microstructures.
- Shear band deformation is closely related to the stress state in a material. For the Copper-oriented crystal with an aspect ratio of 0.5, under a plane strain state with free edges perpendicular to ED, activation of the shear band systems is associated with curvature of the free boundaries. If the edges perpendicular to ED are constrained to maintain straight during deformation, shear bands are localized between the left and right bounding edges and form an angle of 30–45° to ED. The boundary conditions applied in the latter case grossly mimic microstructural effects in a deformed crystal consisting of twin-matrix lamellae. Therefore, the predicted configuration of shear bands (e.g.

decreasing inclination angle and thickening of the bands with deformation, kinks of the first family of bands when intersecting the second family) well captures the experimental observations in low SFE fcc crystals with the same initial orientation.

## Acknowledgements

We gratefully acknowledge the financial support of the National Natural Science Foundation of China (Grant No. 51101030), the Fundamental Research Funds for the Central Universities (Grants Nos. N090302001 and N090202001), and the Foundation for the Youth Teachers from the Ministry of Education of China (Grant No. 20090042120007). The authors are also grateful to the kind support of the Alexander von Humboldt Stiftung (AvH, Alexander von Humboldt Foundation, [www.humboldt-foundation.de](http://www.humboldt-foundation.de)) for N. Jia.

## References

- [1] Duggan BJ, Hatherly M, Hutchinson WB, Wakefield PT. *Metal Sci* 1978;12:343.
- [2] Hutchinson JW, Tvergaard V. *Int J Solids Struct* 1981;17:451.
- [3] Peirce D, Asaro RJ, Needleman A. *Acta Metall* 1983;31:1951.
- [4] Hirsch J, Lücke K. *Acta Metall* 1988;36:2863.
- [5] Donadille C, Valle R, Dervin P, Penelle R. *Acta Metall* 1989;37:1547.
- [6] Tvergaard V, Needleman A. *Proc Roy Soc Lond A* 1993;443:547.
- [7] Batra RC, Zhu ZG. *Acta Mech* 1995;113:185.
- [8] Paul H, Driver JH, Maurice C, Jasieński Z. *Mater Sci Eng A* 2003;359:178.
- [9] Dorner D, Adachi Y, Tsuzaki K. *Scripta Mater* 2007;57:775.
- [10] Hirsch J, Lücke K, Hatherly M. *Acta Metall* 1988;36:2905.
- [11] Köhlhoff GD, Malin AS, Lücke K, Hatherly M. *Acta Metall* 1988;36:2841.
- [12] Leffers T, Ray RK. *Prog Mater Sci* 2009;54:351.
- [13] Paul H, Driver JH, Jasieński Z. *Acta Mater* 2002;50:815.
- [14] Paul H, Driver JH, Maurice C, Piątkowski A. *Acta Mater* 2007;55:575.
- [15] Leffers T, Bilde-Sørensen JB. *Acta Metall Mater* 1991;38:1917.
- [16] Grewen J, Noda T, Sauer D. *Z Metallkd* 1977;68:260.
- [17] Korbel A, Embury JD, Hatherly M, Martin PL, Erbsloh HW. *Acta Metall* 1986;34:1999.
- [18] Morii K, Mecking H, Nakayama Y. *Acta Metall* 1985;33:379.
- [19] Paul H, Morawiec A, Piątkowski A, Bouzy E, Fundenberger J. *Metall Mater Trans A* 2004;35:3775.
- [20] Hong CS, Tao NR, Huang X, Lu K. *Acta Mater* 2010;58:3103.
- [21] Xiao GH, Tao NR, Lu K. *Mater Sci Eng A* 2009;513–514:13.
- [22] Anand L, Spitzig WA. *J Mech Phys Solids* 1980;28:113.
- [23] Bronkhorst CA, Kalidindi SR, Anand L. *Philos Trans Roy Soc Lond A* 1992;341:443.
- [24] Kalidindi SR, Bronkhorst CA, Anand L. *J Mech Phys Solids* 1992;40:537.
- [25] Beaudoin AJ, Dawson PR, Mathur KK, Kocks UF, Korzekwa DA. *Comput Methods Appl Mech Eng* 1994;117:49.
- [26] Becker R, Panchanadeeswaran S. *Acta Metall Mater* 1995;43:2701.
- [27] Dawson PR, Marin EB. *Adv Appl Mech* 1998;34:77.
- [28] Staroselsky A, Anand L. *J Mech Phys Solids* 1998;46:671.
- [29] Kalidindi SR. *J Mech Phys Solids* 1998;46:267.
- [30] Raabe D, Sachtleber M, Zhao Z, Roters F, Zaefferer S. *Acta Mater* 2001;49:3433.
- [31] Raabe D, Zhao Z, Mao W. *Acta Mater* 2002;50:4379.
- [32] Baczmanski A, Braham C. *Acta Mater* 2004;52:1133.

- [33] Raabe D, Roters F. *Int J Plast* 2004;20:339.
- [34] Roters F, Eisenlohr P, Hantcherli L, Tjahjanto DD, Bieler TR, Raabe D. *Acta Mater* 2010;58:1152.
- [35] Dillamore IL, Roberts JG, Bush AC. *Metal Sci* 1979;13:73.
- [36] Van Houtte P, Sevillano JG, Aernoudt E. *Z Metallkd* 1979;70:426.
- [37] Mahesh S. *Acta Mater* 2006;54:4565.
- [38] Mahesh S, Tomé CN. *Philos Mag* 2004;84:3517.
- [39] Mirkhani H, Joshi SP. *Acta Mater* 2011;59:5603.
- [40] Paul H, Morawiec A, Driver JH, Bouzy E. *Int J Plast* 2009;25:1588.
- [41] Jia N, Roters F, Eisenlohr P, Kords C, Raabe D. *Acta Mater* 2012;60:1099.
- [42] Anand L, Su C. *J Mech Phys Solids* 2005;53:1362.
- [43] Kalidindi SR. *Int J Plast* 2001;17:837.
- [44] Blum W, Eisenlohr P. *Mater Sci Eng A* 2009;510–511:7.
- [45] Roters F. Habilitation thesis. Germany: RWTH Aachen University; 2011.
- [46] Kubin L, Devincere B, Hoc T. *Acta Mater* 2008;56:6040.
- [47] Mahajan S, Chin GY. *Acta Metall* 1973;21:1353.
- [48] Wei Y, Su C, Anand L. *Acta Mater* 2006;54:3177.
- [49] El-Danaf E, Kalidindi SR, Doherty RD. *Int J Plast* 2001;17:1245.
- [50] Kuroda M, Tvergaard V. *Int J Plast* 2007;23:244.
- [51] Liu Q, Wert J, Hansen N. *Acta Mater* 2000;48:4267.
- [52] Wert J. *Acta Mater* 2002;50:3127.
- [53] Ferry M, Humphreys FJ. *Mater Sci Eng A* 2006;435–436:447.
- [54] Paul H, Maurice C, Driver JH. *Acta Mater* 2010;58:2799.
- [55] Akef A, Driver JH. *Mater Sci Eng A* 1991;132:245.
- [56] Raabe D, Zhao Z, Roters F. *Scripta Mater* 2004;50:1085.
- [57] Raabe D, Zhao Z, Park SJ, Roters F. *Acta Mater* 2002;50:421.
- [58] Raabe D, Ma D, Roters F. *Acta Mater* 2007;55:4567.